

PROCEEDINGS OF SPIE

EMLC 2008



24th European Mask and Lithography Conference

Uwe F. W. Behringer
Chair/Editor

Wilhelm Maurer
Jacques Waelpoel
Program Chairs

21–24 January 2008
Dresden, Germany

Organized by



VDE/VDI GMM—The Society for Microelectronics,
Micro- and Precision Engineering (Germany)

Cooperating Organizations

BACUS • Photomask Japan (Japan) • SEMI
SPIE • UBC Microelectronics (Germany)

Published by
SPIE

Volume 6792

Proceedings of SPIE, 0277-786X, v. 6792

SPIE is an international society advancing an interdisciplinary approach to the science and application of light.

The papers included in this volume were part of the technical conference cited on the cover and title page. Papers were selected and subject to review by the editors and conference program committee. Some conference presentations may not be available for publication. The papers published in these proceedings reflect the work and thoughts of the authors and are published herein as submitted. The publisher is not responsible for the validity of the information or for any outcomes resulting from reliance thereon.

Please use the following format to cite material from this book:

Author(s), "Title of Paper," in *24th European Mask and Lithography Conference*, edited by Uwe F. W. Behringer, Proceedings of SPIE Vol. 6792 (SPIE, Bellingham, WA, 2008) Article CID Number.

ISSN 0277-786X

ISBN 9780819469564

Published by

SPIE

P.O. Box 10, Bellingham, Washington 98227-0010 USA

Telephone +1 360 676 3290 (Pacific Time) · Fax +1 360 647 1445

SPIE.org

Copyright © 2008, Society of Photo-Optical Instrumentation Engineers

Copying of material in this book for internal or personal use, or for the internal or personal use of specific clients, beyond the fair use provisions granted by the U.S. Copyright Law is authorized by SPIE subject to payment of copying fees. The Transactional Reporting Service base fee for this volume is \$18.00 per article (or portion thereof), which should be paid directly to the Copyright Clearance Center (CCC), 222 Rosewood Drive, Danvers, MA 01923. Payment may also be made electronically through CCC Online at copyright.com. Other copying for republication, resale, advertising or promotion, or any form of systematic or multiple reproduction of any material in this book is prohibited except with permission in writing from the publisher. The CCC fee code is 0277-786X/08/\$18.00.

Printed in the United States of America.

Publication of record for individual papers is online in the SPIE Digital Library.

The logo for SPIE Digital Library features the word "SPIE" in a bold, sans-serif font above the words "Digital Library" in a similar font. To the right of the text is a stylized graphic consisting of three vertical bars of varying heights, with a curved line arching over them.

SPIDigitalLibrary.org

Paper Numbering: Proceedings of SPIE follow an e-First publication model, with papers published first online and then in print and on CD-ROM. Papers are published as they are submitted and meet publication criteria. A unique, consistent, permanent citation identifier (CID) number is assigned to each article at the time of the first publication. Utilization of CIDs allows articles to be fully citable as soon they are published online, and connects the same identifier to all online, print, and electronic versions of the publication. SPIE uses a six-digit CID article numbering system in which:

- The first four digits correspond to the SPIE volume number.
- The last two digits indicate publication order within the volume using a Base 36 numbering system employing both numerals and letters. These two-number sets start with 00, 01, 02, 03, 04, 05, 06, 07, 08, 09, 0A, 0B ... 0Z, followed by 10-1Z, 20-2Z, etc.

The CID number appears on each page of the manuscript. The complete citation is used on the first page, and an abbreviated version on subsequent pages. Numbers in the index correspond to the last two digits of the six-digit CID number.

Contents

- ix Conference Committees
- xiii Foreword
- xvii Conference Supporters
- xix Best Paper from PMJ 2007
Progress of NIL template making (Invited Paper) [6607-124]
S. Yusa, T. Hiraka, A. Kobiki, S. Sasaki, K. Itoh, N. Toyama, M. Kurihara, H. Mohri, N. Hayashi,
Dai Nippon Printing Co., Ltd. (Japan)
- xvii 3-Dimensional bridged structures by thermal-UV imprint using a novel mask (Invited Paper)
[Abstract Only]
K. Okuda, H. Kawata, Y. Hirai, Osaka Prefecture Univ. (Japan)
- xxix Best Paper of BACUS 2007
Polarization-induced astigmatism caused by topographic masks (Invited Paper) [6730-63]
J. Ruoff, J. T. Neumann, Carl Zeiss SMT AG (Germany); E. Schmitt-Weaver, ASML US, Inc.
(USA); E. van Stetten, N. le Masson, ASML Netherlands B.V. (Netherlands); C. Proglor,
Photronics Inc. (USA); B. Geh, Carl Zeiss SMT AG (Germany) and ASML US, Inc. (USA)
- xliv Best Poster of BACUS 2007
*Practical use of hard mask process to fabricate fine photomasks for 45nm node and
beyond (Invited Paper) [6730-147]*
Y. Kushida, H. Handa, H. Maruyama, Fujitsu Ltd. (Japan); Y. Abe, Y. Fujimura, T. Yokoyama,
Dai Nippon Printing Co., Ltd. (Japan)

PLENARY SESSION

- 6792 02 **Mask industry assessment trend analysis [6792-01]**
G. Shelden, Shelden Consulting (USA); P. Marmillion, G. Hughes, SEMATECH (USA)

DOUBLE PATTERNING

- 6792 03 **Double exposure technology for KrF lithography [6792-06]**
S. Geisler, J. Bauer, U. Haak, IHP Microelectronics (Germany); D. Stolarek, Technische
Fachhochschule Wildau (Germany); K. Schulz, IHP Microelectronics (Germany); H. Wolf,
Photonics MZD GmbH (Germany); W. Meier, Nikon Precision Europe GmbH (Germany);
M. Trojahn, Rohm and Haas Electronic Materials Deutschland GmbH (Germany); E.
Matthus, IHP Microelectronics (Germany); H. Beyer, Technische Fachhochschule Wildau
(Germany); G. Old, Nikon Precision Europe GmbH (Germany); St. Marschmeyer, B. Kuck,
IHP Microelectronics (Germany)

- 6792 04 **Wafer based mask characterization for double patterning lithography** [6792-07]
R. de Kruijf, ASML Netherlands B.V. (Netherlands); K. Bubke, Advanced Mask Technology Ctr. GmbH & Co. KG (Germany); G.-J. Janssen, E. van der Heijden, ASML Netherlands B.V. (Netherlands); J. Fochler, Toppan Photomasks, Inc. (Germany); M. Dusa, ASML US Inc. (USA); J. H. Peters, Advanced Mask Technology Ctr. GmbH & Co. KG (Germany); P. de Haas, ASML Netherlands B.V. (Netherlands); B. Connolly, Toppan Photomasks, Inc. (Germany)
- 6792 05 **Topological and model based approach to pitch decomposition for double patterning** [6792-08]
P. Nikolsky, N. Davydova, ASML Netherlands B.V. (Netherlands); R. Goossens, Brion Technologies, an ASML Company (USA)

SIMULATION

- 6792 06 **Fast rigorous simulation of mask diffraction using the waveguide method with parallelized decomposition technique** [6792-09]
F. Shao, P. Evanschitzky, D. Reibold, A. Erdmann, Fraunhofer Institute of Integrated Systems and Device Technology (Germany)
- 6792 07 **Three dimensional mask effects in OPC process model development from first principles simulation** [6792-10]
L. S. Melvin III, Synopsys, Inc. (USA); T. Schmoeller, C. K. Kalus, Synopsys GmbH (Germany); J. Li, Synopsys, Inc. (USA)

MASK BUSINESS AND MASK DATA PREP

- 6792 08 **Key improvement schemes of accuracies in EB mask writing for double patterning lithography** [6792-11]
H. Sunaoshi, T. Kamikubo, R. Nishimura, K. Tsuruta, T. Katsumata, T. Ohnishi, H. Anze, J. Takamatsu, S. Yoshitake, S. Tamamushi, NuFlare Technology, Inc. (Japan)
- 6792 09 **Mask data rank (MDR) and its application** [6792-12]
K. Kato, M. Endo, T. Inoue, M. Yamabe, Association of Super-Advanced Electronics Technologies (Japan)
- 6792 0A **MEDEA+ project 2T302 MUSCLE: masks through user's supply chain: leadership by excellence** [6792-13]
A. Torsy, Altis Semiconductor (France) and Infineon Technologies AG (Germany)
- 6792 0B **Printing of sub-resolution shots in electron beam direct write with variable shaped beam machines** [6792-14]
F. Thrum, J. Kretz, C. Hohle, K.-H. Choi, Qimonda Dresden GmbH & Co. OHG (Germany); K. Keil, Fraunhofer Ctr. for Nanoelectronic Technologies (Germany)

MASK CLEANING / HAZE

- 6792 0C **Assessment of molecular contamination in mask pod** [6792-15]
J. M. Foray, Alcatel Vacuum Technology (France); P. Dejaune, P. Sergent, Toppan Photomasks (France); S. Gough, STMicroelectronics (France); D. Cheung, Entegris Cleaning Process S.A.S. (France); M. Davenet, A. Favre, C. Rude, T. Trautmann, Alcatel Vacuum Technology (France); M. Tissier, Toppan Photomasks (France); H. Fontaine, M. Veillerot, CEA-LETI, MINATEC (France); K. Avary, I. Hollein, R. Lerit, Advanced Mask Technology Ctr. GmbH & Co. KG (Germany)
- 6792 0D **Photomask cleaning process improvement to minimize ArF haze** [6792-16]
M. Graham, A. McDonald, Photronics (UK) Ltd. (United Kingdom)
- 6792 0E **Theoretical study of mask haze formation** [6792-17]
B. Wu, A. Kumar, Applied Materials, Inc. (USA)

INSPECTION AND REPAIR

- 6792 0F **EUV blank inspection** [6792-18]
J. H. Peters, C. Tonk, Advanced Mask Technology Ctr. (Germany); D. Spriegel, Siemens AG (Germany); H.-S. Han, W. Cho, S. Wurm, SEMATECH (USA)
- 6792 0G **Introduction of new database reflected tritone algorithm for application in mask production** [6792-19]
T. Schulmeyer, Advanced Mask Technology Ctr. (Germany); H. Schmalfluss, KLA-Tencor GmbH (Germany); J. Heumann, Advanced Mask Technology Ctr. (Germany); M. Lang, KLA-Tencor GmbH (Germany)
- 6792 0H **Phase-shifting photomask repair and repair validation procedure for transparent and opaque defects relevant for the 45nm node and beyond** [6792-20]
C. Ehrlich, U. Buttgerit, K. Boehm, T. Scheruebl, Carl Zeiss SMS GmbH (Germany); K. Edinger, T. Bret, Nawotec GmbH, a Carl Zeiss SMS GmbH Company (Germany)
- 6792 0I **Inspection results of advanced (sub-50nm design rule) reticles using the TeraScanHR** [6792-21]
J.-P. Sier, W. Broadbent, P. Yu, KLA-Tencor Corp. (USA)

RESIST

- 6792 0J **Alternative approach to transparent stamps for UV-based nanoimprint lithography: techniques and materials** [6792-22]
A. Klukowska, M. Vogler, A. Kolander, F. Reuther, G. Gruetzner, micro resist technology GmbH (Germany); M. Muehlberger, I. Bergmair, R. Schoeffner, Profactor Produktionsforschungs GmbH (Austria)

METROLOGY

- 6792 OK **Characterizing the imaging performance of flash memory masks using AIMS** [6792-23]
E. van Setten, O. Wismans, K. Grim, J. Finders, ASML Netherlands B.V. (Netherlands);
M. Dusa, ASML TDC (USA); R. Birkner, R. Richter, T. Scherübl, Carl Zeiss SMS GmbH (Germany)
- 6792 OL **CDO budgeting** [6792-24]
P. Nesladek, A. Wiswesser, B. Sass, S. Mauermann, Advanced Mask Technology Ctr.
(Germany)
- 6792 OM **High-resolution and high-precision pattern placement metrology for the 45 nm node and beyond** [6792-25]
G. Klose, Carl Zeiss SMT AG (Germany); U. Buttgereit, Carl Zeiss SMS GmbH (Germany);
M. Arnz, Carl Zeiss SMT AG (Germany); N. Rosenkranz, Carl Zeiss SMS GmbH (Germany)
- 6792 ON **Mask CD measurement approach by diffraction intensity for lithography equivalent**
[6792-26]
T. Nagai, K. Mesuda, T. Sutou, Y. Inazuki, H. Hashimoto, T. Yokoyama, N. Toyama,
Y. Morikawa, H. Mohri, N. Hayashi, Dai Nippon Printing Co., Ltd. (Japan)
- 6792 OO **Influences on accuracy of SEM based CD mask metrology with a view to the 32 nm node**
[6792-27]
W. Häßler-Grohne, C. G. Frase, D. Gnieser, H. Bosse, Physikalisch-Technische Bundesanstalt
(Germany); J. Richter, A. Wiswesser, Advanced Mask Technology Ctr. (Germany)
- 6792 OP **Comparative scatterometric CD and edge profile measurements on a MoSi mask using different scatterometers** [6792-28]
M. Wurm, A. Diener, B. Bodermann, Physikalisch-Technische Bundesanstalt (Germany)

RET

- 6792 OQ **Assessment and application of focus drilling for DRAM contact hole fabrication** [6792-38]
C. Noelscher, F. Jauzion-Graverolle, T. Henkel, Qimonda Dresden GmbH & Co. OHG
(Germany)
- 6792 OR **Design of pattern-specific mask grating for giving the effect of an off-axis illumination**
[6792-39]
Y.-S. Kim, Inha Univ. (South Korea); S. H. Song, Hanyang Univ. (South Korea); J. U. Lee,
Cheongju Univ. (South Korea); S. H. Oh, Y. K. Choi, M. Kim, Hynix Semiconductor Inc. (South
Korea); B.-H. O, S.-G. Park, E.-H. Lee, S. G. Lee, Inha Univ. (South Korea)
- 6792 OS **Overcoming mask etch challenges for 45 nm and beyond** [6792-40]
M. Chandrachood, T. Y. B. Leung, K. Yu, M. Grimbergen, S. Panayil, I. Ibrahim,
A. Sabharwal, A. Kumar, Applied Materials, Inc. (USA)

EUV I

- 6792 OT **Desired IP control methodology for EUV mask in current mask process** [6792-41]
S. Yoshitake, H. Sunaoshi, S. Tamamushi, NuFlare Technology, Inc. (Japan); M. Ogasawara,
Toshiba Corp. (Japan)

- 6792 0U **Use of EUV scatterometry for the characterization of line profiles and line roughness on photomasks** [6792-42]
F. Scholze, C. Laubis, Physikalisch-Technische Bundesanstalt (Germany)

NIL

- 6792 0V **Strategies for hybrid techniques of UV lithography and thermal nanoimprint** [6792-43]
M. Wissen, N. Bogdanski, S. Moellenbeck, H.-C. Scheer, Univ. of Wuppertal (Germany)
- 6792 0W **Controlling linewidth roughness in step and flash imprint lithography (Best Paper Award)** [6792-44]
G. M. Schmid, N. Khusnatdinov, C. B. Brooks, D. L. LaBrake, E. Thompson, D. J. Resnick, Molecular Imprints, Inc. (USA); J. Owens, A. Ford, SEMATECH (USA); S. Sasaki, N. Toyama, M. Kurihara, N. Hayashi, Dai Nippon Printing Co., Ltd. (Japan); H. Kobayashi, T. Sato, O. Nagarekawa, Hoya Corp. (Japan); M. W. Hart, K. Gopalakrishnan, R. Shenoy, R. Jih, IBM Almaden Research Ctr. (USA); Y. Zhang, E. Sikorski, M. B. Rothwell, IBM Thomas J. Watson Research Ctr. (USA); S. Yoshitake, H. Sunaoshi, K. Yasui, NuFlare Technology, Inc. (Japan)

EUL II

- 6792 0X **Status of EUVL reticle chucking** [6792-45]
R. L. Engelstad, Univ. of Wisconsin, Madison (USA); J. Sohn, SEMATECH (USA); J. R. Zeuske, V. S. Battula, P. Vukkadala, Univ. of Wisconsin, Madison (USA); C. K. Van Peski, K. J. Orvek, SEMATECH (USA); K. T. Turner, A. R. Mikkelson, M. Nataraju, Univ. of Wisconsin, Madison (USA)
- 6792 0Y **45nm node registration metrology on LTEM EUV reticles** [6792-46]
F. Laske, Vistec Semiconductor Systems GmbH (Germany); H. Kinoshita, N. Nishida, D. Kenmochi, Hoya Corp. (Japan); H. Ota, Y. Tanioka, Dai Nippon Screen Manufacturing Co., Ltd. (Japan); S. Czerkas, K.-H. Schmidt, D. Adam, K.-D. Roeth, Vistec Semiconductor Systems GmbH (Germany)

POSTER SESSION

- 6792 0Z **Top surface imaging study by selective chemisorptions of poly(dimethyl siloxane) on diazoketo-functionalized polymeric surface** [6792-29]
R. Ganesan, S. K. Youn, J.-M. Yun, J.-B. Kim, Korea Advanced Institute of Science and Technology (South Korea)
- 6792 10 **Optical proximity correction for 0.13 μm SiGe:C BiCMOS** [6792-30]
S. Geisler, Technische Fachhochschule Wildau (Germany) and IHP Microelectronics (Germany); J. Bauer, U. Haak, U. Jagdhold, R. Pliqueff, E. Matthus, IHP Microelectronics (Germany); R. Schrader, H. Wolf, Photronics MZD GmbH (Germany); U. Baetz, Fraunhofer IPMS (Germany); H. Beyer, Technische Fachhochschule Wildau (Germany); M. Niehoff, Mentor Graphics (Germany)

- 6792 11 **New alignment marks for improved measurement maturity** [6792-31]
U. Weidenmueller, H. Alves, B. Schnabel, Vistec Electron Beam GmbH (Germany); B. Icard, L. Pain, CEA-LETI, MINATEC (France); J.-C. Le-Denmat, S. Manakli, STMicroelectronics (France); J. Pradelles, CEA-LETI, MINATEC (France)
- 6792 12 **Measuring contact hole corner rounding uniformity using optical scatterometry** [6792-32]
J. C. Lam, n&k Technology, Inc. (USA); A. Gray, Univ. of California at Davis (USA); S. Chen, n&k Technology, Inc. (USA); J. Richter, Advanced Mask Technology Ctr. GmbH & Co. KG (Germany)
- 6792 13 **Very high sensitivity mask DUV transmittance mapping and measurements based on non-imaging optics (Best Poster Paper Award)** [6792-33]
G. Ben-Zvi, V. Dmitriev, E. Graitzer, E. Zait, O. Sharoni, A. Cohen, Pixar Technology Ltd. (Israel)
- 6792 14 **Advances in fabrication of x-ray masks based on vitreous carbon using a new UV sensitive positive resist** [6792-34]
A. Voigt, micro resist technology GmbH (Germany); J. Kouba, BESSY GmbH (Germany); M. Heinrich, G. Gruetzner, micro resist technology GmbH (Germany); H.-U. Scheunemann, I. Rudolph, C. Waberski, BESSY GmbH (Germany)
- 6792 15 **New results from DUV water immersion microscopy using the CD metrology system LWM500 WI with a high NA condenser** [6792-35]
F. Hillmann, G. Scheuring, H.-J. Brück, MueTec GmbH (Germany)
- 6792 16 **High resolution patterning and simulation on Mo/Si multilayer for EUV masks** [6792-36]
N. Tsirikas, G. P. Patsis, I. Raptis, Institute of Microelectronics, NCSR Demokritos (Greece); A. Gerardino, Istituto di Fotonica e Nanotecnologie, CNR (Italy)
- 6792 17 **Phame: high resolution off-axis phase shift measurements on 45nm node features** [6792-37]
U. Buttgerit, S. Perlitz, D. Seidel, Carl Zeiss SMS GmbH (Germany)

Author Index

Conference Committees

European Mask and Lithography International Steering Committee and European Mask and Lithography Conference Program Committee (*)

Conference Chair

Uwe F. W. Behringer*, UBC Microelectronics (Germany)

Program Chairs

Wilhelm Maurer*, Infineon Technologies AG (Germany)

Jacques A. Waelpoel*, ASML Netherlands B.V. (Netherlands)

Members

F. Abboud, Intel Corporation (USA)

M. Arnz*, Carl Zeiss SMT AG (Germany)

E. Baracchi, ST Microelectronics (Italy)

C. Blaesing, Carl Zeiss SMS GmbH (Germany)

P. Chen*, Taiwan Mask Corporation (Taiwan)

C. Constantine*, Oerlikon USA Inc. (USA)

R. Engelstad*, University of Wisconsin, Madison (USA)

B. G. Eynon*, SEMATECH-Samsung Assignee (USA)

D. Farrar, Hoya Corporation (United Kingdom)

M. Fischer, KLA Tencor GmbH (Germany)

O. Fortagne, Vistec Semiconductor Systems GmbH (Germany)

C. Gale*, Applied Materials (Germany)

B. Grenon*, Grenon Consulting, Inc (USA)

H. Hartmann, S3 Solutions (Germany)

N. Hayashi*, Dai Nippon Printing Company Ltd. (Japan)

A. C. Hourd*, Compugraphics International Ltd. (United Kingdom)

R. Jonckheere*, IMEC (Belgium)

C. K. Kalus*, Synopsys GmbH (Germany)

K. R. Kimmel*, AMTC (Germany)

B. Lauche, Photonics MZD GmbH (Germany)

H. Lehon, KLA-Tencor Corporation (USA)

H. Loeschner*, IMS Nanofabrication AG (Austria)

B. Naber*, Cadence Design Systems Inc. (USA)

J. Perrocheau, JEMI-France (France)

Ch. Pierrat*, Cadence Design Systems Inc. (USA)

E. Rausa*, Oerlikon USA Inc. (USA)

D. J. Resnick*, Molecular Imprints (USA)

F. Reuther, micro resist technology GmbH (Germany)

C. Romeo*, ST Microelectronics (Italy)
K. Ronse, IMEC (Belgium)
H. Scheer*, University of Wuppertal (Germany)
G. Scheuring, Mue Tec GmbH (Germany)
R. Schnabel*, VDE/VDI-GMM (Germany)
M. Staples, AMD Saxony LLC & Company KG (Germany)
I. Stolberg*, Vistec Electron Beam GmbH (Germany)
S. Tedesco*, CEA-LETI, Grenoble (France)
M. Tissier*, Toppan Photomasks S.A. (France)
G. Unger*, Qimonda GmbH & Company OHG (Germany)
J. T. Weed, Synopsys, Inc. (USA)
J. Whittey*, Vistec Semiconductor Systems (USA)
J. Wiley, Brion Technologies (USA)
H. Wolf*, Photronics MZD GmbH (Germany)
N. Yoshioka, Renesas Technology Corporation (Japan)
L. Zurbrick*, Agilent Technologies (USA)

Session Chairs

Plenary Session I

Uwe F. W. Behringer, UBC Microelectronics (Germany)
Wilhelm Maurer, Infineon Technologies AG (Germany)

Plenary Session II

Wilhelm Maurer, Infineon Technologies AG (Germany)
Jacques A. Waelpoel, ASML Netherlands B.V. (Netherlands)

Double Patterning

Michael Arnz, Carl Zeiss SMT AG (Germany)
Peter Nikolsky, ASML Netherlands B.V. (Netherlands)

Simulation

Christian Kalus, Synopsys GmbH (Germany)
Wilhelm Maurer, Infineon Technologies AG (Germany)

Mask Business and Mask Data Prep

Hermann Wolf, Photronics MZD GmbH (Germany)
Michel Tissier, Toppan Photomask S.A. (France)

Mask Cleaning / Haze

Brian Grenon, Grenon Consulting, Inc. (USA)
Naoyo Hayashi, Dai Nippon Printing Company Ltd. (Japan)

Inspection and Repair

Michael Archuleta, RAVE LLC Nanomachining (USA)
Gerd Unger, Qimonda GmbH & Company OHG (Germany)

Resist

Freimuth Reuther, micro resist technology GmbH (Germany)

Hella Scheer, University of Wuppertal (Germany)

Metrology

John Whittey, Vistec Semiconductor Systems (USA)

Carola Blaesing, Carl Zeiss SMS GmbH (Germany)

RET

Rik Jonckheere, IMEC (Belgium)

Ines Stolberg, Vistec Electron Beam GmbH (Germany)

EUV I

Kurt R. Kimmel, AMTC (Germany)

Roxann Engelstad, University of Wisconsin, Madison (USA)

NIL

Hella Scheer, University of Wuppertal (Germany)

Douglas J. Resnick, Molecular Imprints (USA)

EUL II

Serge Tedesco, CEA-LETI, Grenoble (France)

Ben G. Eynon, SEMATECH-Samsung Assignee (USA)

Poster Session

Chris Gale, Applied Materials (Germany)

Uwe F. W. Behringer, UBC Microelectronics (Germany)

Foreword

The EMLC Has Returned to Dresden, Germany

In 2007, the 23rd European Mask and Lithography Conference (EMLC2007) took place in Grenoble, France. It was the first time in its 23-year history that the EMLC was held outside Germany. The VDE/VDI-GMM and the EMLC Organizing Committee were invited to Grenoble, France during last year's conference in Dresden by CEA/LETI, MINATEC, and Toppan Photomasks.

For 2008, the 24th Mask and Lithography Conference (EMLC2008) came back to Dresden. EMLC2008 was held on 21–24 January 21st 2008, at the Hilton Hotel in Dresden, Germany. As in the past years, the conference brought together scientists, researchers, engineers, and technologists from research institutes and companies around the world to present papers at the forefront of mask lithography and mask technology.

The three-day conference is dedicated to the science, technology, engineering and application of mask and lithography technologies and associated processes, and gives an overview of the present status in mask and lithography technologies and the future strategy where mask producers and users have the opportunity to become acquainted with new developments and results. This year's session topics included Double Patterning, Simulation, Mask Business & Mask Data Prep, Mask Cleaning & Haze, Inspection & Repair, Resist, Metrology, RET, EUV, and NIL. A small poster session was also included.

There were a total of 254 conference attendees at the EMLC2008. This number includes the 25 exhibitors from the Technical Exhibition. The largest share of attendees (136) came from Germany, 33 came from the USA, 23 from France, 19 from Japan and 12 from the Netherlands. These were the five largest groups by nationality in attendance. About 55% of the contributions came from Europe and about 45% from outside Europe. The largest number of papers submitted, by nationality, were from Germany (22), the USA (10), and Japan (8). In total we had 63 different companies participating in papers as authors or co-authors. We feel this participation demonstrates worldwide cooperation in the lithography and photomask community.

Highlights of the EMLC2008

The keynote speaker of EMLC2008 was Steve McDonald, the Central Mask Integration Manager of Photronics NanoFab in Boise, Idaho, USA. Steve gave a talk about the challenges in mask making today. Here are some excerpts from his presentation:

"Semiconductor manufacturing is changing more rapidly than ever before, and our industry faces enormous near-term challenges as we move forward into high NA 193 immersion, double patterning, and double exposure lithography. For mask makers the challenges at the 32 nm node and beyond are extremely difficult. Huge data volumes, long write times, and more challenging OPC, coupled with low single-digit specifications for CD control, increasingly tight pattern placement and plate to plate overlay requirements, and ever smaller defect specifications."

"As Moore's law continues to drive node reduction and progress in our industry, the challenges will not lessen, but through the dedication and innovation of you and your colleagues, our industry will continue to meet the requirements. The incredible advancement in the end user products enabled by this innovation, the cell phones, PDAs, PCs, laptops, televisions, gaming stations, automotive navigation and safety systems, etc. are all tangible examples of the work you do every day. These products are the leading users of semiconductor output, and as we know all too well, they have relatively short product life cycles. To keep new and exciting offerings in front of the consumer, the product manufacturers must pack more and more functionality into the same or smaller sized packages, all the while making them faster, cheaper and run cooler than ever before. This continual improvement cycle drives our industry, requiring semiconductor advancements at a rate previously not experienced."

Greg Hughes from SEMATECH, Austin, TX, USA stated in his presentation entitled "Mask Industry Assessment Trend Analysis" that logic designs are driving the majority of mask volume. Looking at year-to-year responses, this percentage has trended down from 70% in 2002 to 43% in 2007. From a mask volume standpoint, memory and microprocessor volumes are low and stable given the change in participants with an average volume of 10.8% and 3.4%, respectively.

Mask technologies for the sub-130 nm node have risen to 17% of the mask volume; 60% of all masks are still built to a 250 nm or larger design node. The sub-65 nm node technology is now 2.8% of the mask volume. Currently 70% of photomasks are made on a 6025 format. Over the last five years, this percentage has slowly increased.

As in the past, the major process-related yield loss mechanisms are basically constant year to year. Hard defects account for nearly half of the yield loss for the five-year period. Human error (administrative and manufacturing errors combined) accounts for approximately 20% of yield losses. CD control is surprisingly low at 15%.

Who are the potential lithography candidates for the 32 nm node?

Out of the presentations I see at least 3 candidates

- High-n Immersion
- Double Patterning
- the late fellow EUVL

It was also stated that line edge roughness will become a serious problem because not enough photons will arrive to the resist at a high throughput rate of 100 wafers per hour on the proposed exposure tool(s).

Douglas Resnick from Molecular Imprints explained that by using imprint technology this problem will not appear since the line quality is defined by the "template mask" quality where the writing time of the "template mask" can be enlarged several times compared to the writing time of an optical mask. The reason for this: The area exposed by an electron beam writing system is normally four times smaller on a template used for nano-imprint lithography (NIL).

Robert de Kruijff from ASML of the Netherlands, showed in his presentation "Wafer based mask characterization for double patterning lithography" that double patterning technology (DPT) is considered the most acceptable solution for 32 nm node lithography. He mentioned that apart from the obvious drawbacks of additional exposure and

processing steps and therefore reduced throughput, DPT possesses a number of additional technical challenges related to exposure tool capability, the actual applied process in the wafer fab, as well as mask to mask performance. Robert reported on the performance of a two-reticle set based on a design developed to study the impact of mask global and local placement errors on a DPT dual line process. For 32 nm node lithography using DPT, a reticle to reticle overlay measured on the same structures on both masks was found to be smaller or equal to $1.5 \text{ nm } 3\sigma$.

For EUV it was stated that EUV lithography seems to have failed to be inserted for the 32 nm node device production due to delay in overcoming technical challenges. The technical issue ranking in 2007 is unchanged from 2006. That is the reason that some device suppliers announced that they will adopt hi-index immersion lithography with double patterning technique for 32 nm hp device.

Other experts however stated that EUV lithography still has the advantage in resolution capability over other optical lithography technologies and it is strongly expected to be introduced into device production with the extendibility for 2x nm hp generation.

Coming to the champions

The award for the Best Poster of EMLC2008, for "Very high sensitivity mask DUV transmittance mapping and measurements based on non imaging optics" was presented at the Banquet Dinner at the Hilton Hotel to Guy Ben-Zvi, and co-authors, Vladimir Dmitriev, Erez Graitzer, Eitan Zait, Ofir Sharoni, Avi Cohen from Pixar Technology, Israel.

The paper "Controlling linewidth roughness in step and flash imprint lithography" won the Best Paper Award of EMLC2008. This paper was authored by Douglas Resnick from Molecular Imprints, (USA) and co-authors, Gerard M. Schmid, Niyaz Khusnatdinov, Cynthia B. Brooks, Dwayne L. LaBrake, Ecron Thompson, Molecular Imprints, Inc. (USA); Jordan Owens, Arnie Ford, Advanced Technology Development Facility, Inc. (USA); Shiho Sasaki, Nobuhito Toyama, Masaaki Kurihara, Naoya Hayashi, Dai Nippon Printing Co., Ltd. (Japan); Hideo Kobayashi, Takashi Sato, Osamu Nagarekawa, HOYA Corp. (Japan); Mark W. Hart, Kailash Gopalakrishnan, Rohit Shenoy, Ron Jih, IBM Almaden Research Ctr. (USA); Ying Zhang, Edmund Sikorski, Mary Beth Rothwell, IBM Thomas J. Watson Research Ctr. (USA); Shusuke Yoshitake, Hitoshi Sunaoshi, Kenichi Yasui, NuFlare Technology, Inc. (Japan) Douglas Resnick will accept The Best Paper Award during the Banquet at the Photomask Japan 2008 conference in April 2008, in Yokohama, Japan.

The EMLC2008 Program Committee would like to thank Dr. Wilhelm Maurer from Infineon (one of the two program chairs) for organizing the very impressive window tour at Qimonda in Dresden that took place on the third day of the conference.

In 2009 the 25th European Mask and Lithography Conference (EMLC2009) will again be held at the Hilton Hotel in Dresden, Germany. The proposed dates are currently 12–15 January 2009.

Uwe F. W. Behringer

The Steering Committee of the 24th European Mask and Lithography Conference, EMLC would like to express its sincere appreciation to all sponsors and cooperating partners mentioned below for their support.



PROGRESS OF NIL TEMPLATE MAKING

Satoshi Yusa, Takaaki Hiraka, Ayumi Kobiki, Shiho Sasaki, Kimio Itoh, Nobuhito Toyama, Masaaki Kurihara, Hiroshi Mohri, and Naoya Hayashi

Electronic Device Laboratory
Dai Nippon Printing Co., Ltd.
2-2-1 Fukuoka, Fujimino-shi, Saitama, Japan 356-8507

ABSTRACT

Nano-imprint lithography (NIL) has been counted as one of the lithography solutions for hp32nm node and beyond. Recently, the small line edge roughness (LER) as well as the potentially high resolution that will ensure no-OPC mask feature is attracting many researchers. The template making is one of the most critical issues for the realization of NIL. Especially when we think of a practical template fabrication process on a 65mm square format that is going to be the industry standard, the resolution of the template making process showed a limitation.

We have achieved for the first time an hp22nm resolution on the 65nm template format. Both line and space patterns and hole patterns were well resolved. Regarding dot patterns, we still need improvement, but we have achieved resolution down to hp28nm.

Although so far we cannot achieve these resolution limits of various pattern category at the same time on one substrate, an intermediate process condition showed sufficient uniformity both in lateral CD and in vertical depth. Global pattern image placement also showed sufficient numbers at this stage of lithography development.

A 20nm feature (with a pitch of 80nm) showed sufficient imprint result.

Keywords: Nano-imprint, template, resolution, hp22nm

1. INTRODUCTION

Nano-imprint lithography (NIL) is expected as a lithography solution for fine pattern lithography not only for the potentially high resolution that will ensure no-OPC mask feature but also for the potential small line edge roughness (LER). Hp22nm has been a fairly good target for the NIL development, and our development on templates has set the target from the early development stage.

We have been studying about the possibility of practical template fabrication and although it is difficult to apply the technology for full-chip pattern making because of the low speed, we have been using a 100kV spot beam writer for the pattern generation and a non-CAR resist¹⁻⁴. Our trial against faster pattern writing will be reported and discussed in another paper at this symposium⁵. In this paper, we will focus on our target resolution improvement.

2. TEMPLATE MANUFACTURING FLOW

Figure 1 shows an example of our process flow for template manufacturing. A thin chrome, usually with a thickness of 15nm or thinner, is coated between the EB resist and the quartz substrate. The chrome enables us to make the resist thickness thinner, and may also reduce charge up problem during EB writing and resist peeling issues due to poor adhesion between resist and quartz.

A similar process as that for chromeless mask is used to make the fine patterns on the quartz substrate. The substrate is a 6" format for conventional photomasks, and if we can use this size for the imprint process, we can strip the chrome and finalize the template making. Usually, a 65mm square format, as has been introduced by Molecular Imprints, Inc. is used in the imprint process, and for this format, we keep the chrome on the substrate and proceed to the back-end process of template manufacturing.

The back-end process is described in figure 2. First we will form the pattern for the pedestal making by alignment

writing on a re-coated resist. The pedestal is made by wet etch of the surroundings. Next, the dicing and polishing process will cut the 6" plate to four 65mm square plates. Until this process, the chrome and the secondly coated resist remains. After stripping the resist and chrome, the templates will be coated with anti-sticking coatings, if needed.

Table 1 shows the tools and the materials used. A Jeol JBX9300FS (100kV spot beam writer) was used to generate the patterns on the positive tone non-CAR. For metrology, we used CD-SEMs (KLA-8100XPR and Vistec LWM9000), an image placement measurement system (Vistec LMS IPRO), an AFM (Veeco Dimension X3D), and a cross section SEM (Carl Zeiss Ultra system).

3. RESULTS AND DISCUSSION

Fig. 3. shows the results of our previous work. As is shown, from the SEM top view, hp22nm are resolved, but when we etch down the chrome and quartz, our resolution limit was hp28nm.

The key items that are dominant in template resolution are:

- 1) resist material and its thickness,
- 2) hard mask material and its thickness,
- 3) writing tool and its operating condition, and
- 4) resist development and etch process.

In this paper we focused on writing condition and process condition optimization to improve the resolution. For the writing conditions, we tried various CD bias and tested a range of writing dosage. The development condition was optimized to each writing conditions.

Fig. 4. and 5. show the resolution limit exploring result of a "Condition A". The "Condition A" is an improvement of our previous work's conditions and mainly the development condition was improved. We can see the quartz trenches are formed to the hp22nm, but collapsing issues can be seen on the fine features.

Fig. 6. and 7. show the resolution of a "Condition B". To develop the "Condition B", we changed the data bias as well as the writing dosage. We can see that hp22nm is well etched down to the quartz trenches. But we also can see that the lateral CD of larger patterns, such as the hp32nm patterns, is not controlled well. This could be well recognized if we compare the pictures with those of the "Condition A", where we can see better CD controllability.

Fig. 8. shows the resolution improvement result of dense hole patterns. To make the dense hole patterns we employed a "Condition C" that is specialized for holes. Hp22nm dense holes are well formed. Figure x shows the results of dense dot patterns, with a "Condition D" that is optimized for dot pattern making. For dots, we could not achieve hp22nm, and hp28nm is the limit so far.

To summarize the above mentioned results, we could achieve hp22nm for line and space patterns and hole patterns. But still we can not realize hp22nm resolution of various pattern categories at the same time, and we have to use manufacturing conditions that are optimized for each category.

Fig. 9. shows the lateral CD uniformity and depth uniformity in the 35mm square area. The lateral CD was measured at hp32nm pattern, where the line CD was approximately 24nm. The depth was measured on hp100nm pattern, where the trench CD was approximately 100nm. The CD uniformity was 3.1nm in 3σ , and the depth uniformity was 0.53nm in 3σ . These numbers are sufficient number at this point of the development. Figure10 shows the global image placement metrology result in a 35mm square area. The error was kept at a level of less than 8nm.

Fig. 11. shows an imprint result of our template. The imprint was done with a Molecular Imprints, Inc. NIL tool with their materials. We can see that a 20nm fine line (though the pitch is looser here) is well printed. Unfortunately the hp22nm patterns were just developed and were not prepared in time to be imprinted, so we have no results of imprinted patterns at this time. These will be reported in the following chances. The 20nm lines show excellent fidelity and very small LER.

4. SUMMARY

Templates features with hp22nm on line and space patterns and hole patterns were made on the 6" quartz substrate. Dots of hp28nm were also resolved. Although each pattern category has to be made with optimized manufacturing conditions, we are now ready for fine pattern template making.

ACKNOWLEDGEMENT

The authors would like to thank Molecular Imprints, Inc. engineers for the imprint results. We would also thank Yoko Suda and Megumi Kabashima of DNP for their SEM works.

REFERENCES

1. S. Sasaki, K. Itoh, A. Fujii, N. Toyama, H. Mohri, N. Hayashi, "Photomask development for next generation lithography," *Proceeding of SPIE*, vol. 5853, pp.277-288, 2005.
2. S. Sasaki, Y. Yoshida, T. Amano, K. Itoh, N. Toyama, H. Mohri, N. Hayashi, "Patterning process development for NIL template," *GMM Fachbericht*, vol. 49 (22nd European Mask and Lithography Conference,) pp.203-206, 2006.
3. Y. Yoshida, T. Amano, S. Sasaki, K. Itoh, N. Toyama, H. Mohri, N. Hayashi, "Dry etch technology development for NIL template," *Proceeding of SPIE*, vol. 6283, 62833G, 2006.
4. Y. Yoshida, A. Kobiki, T. Hiraka, S. Yusa, S. Sasaki, K. Itoh, N. Toyama, M. Kurihara, H. Mohri, N. Hayashi, "NIL template making and imprint evaluation," *Proceeding of SPIE*, vol. 6349, 63492C, 2006.
5. M. Ishikawa, M. Sakaki, H. Fujita, H. Sano, M. Hoga, N. Hayashi, "Hybrid EB-writing technique with a 50kV-VSB writer and a 100kV-SB writer for NIL mold fabrication," *Proceeding of SPIE*, vol. 6607, to be printed

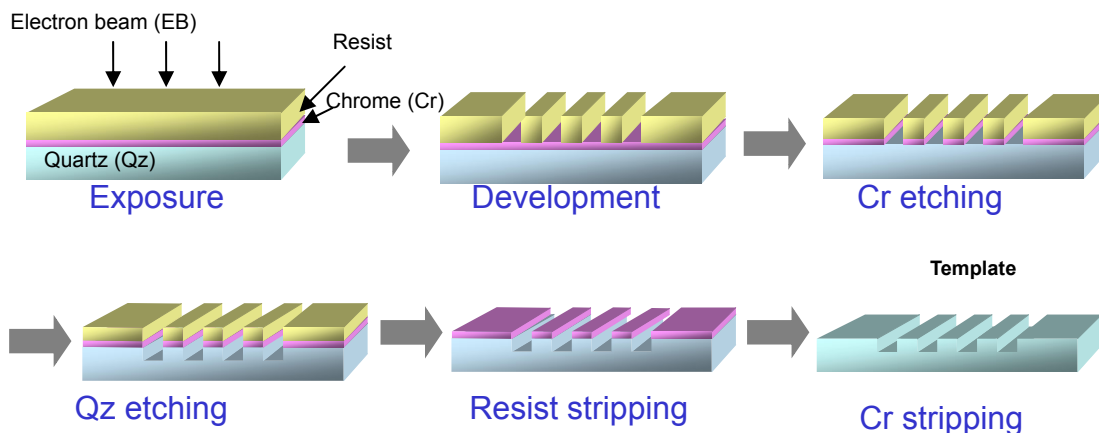


Fig. 1. Process flow of NIL template

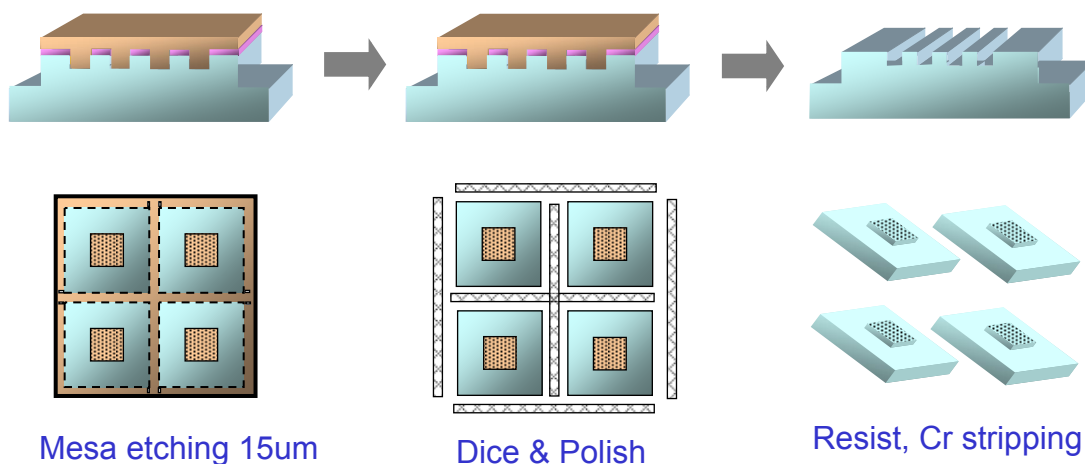


Fig. 2. Process flow of back end process

Table1 Tools and material

Writing tool	JBX9300 (100keV spot beam writer)
Resist material	Non CAR (POSI)
Measurement tools	CD-SEM (KLA-8100XPR, LWM9000)
	Image placement measurement (LMS IPRO)
	AFM (Dimension X3D)
	Cross section-SEM (Ultra)

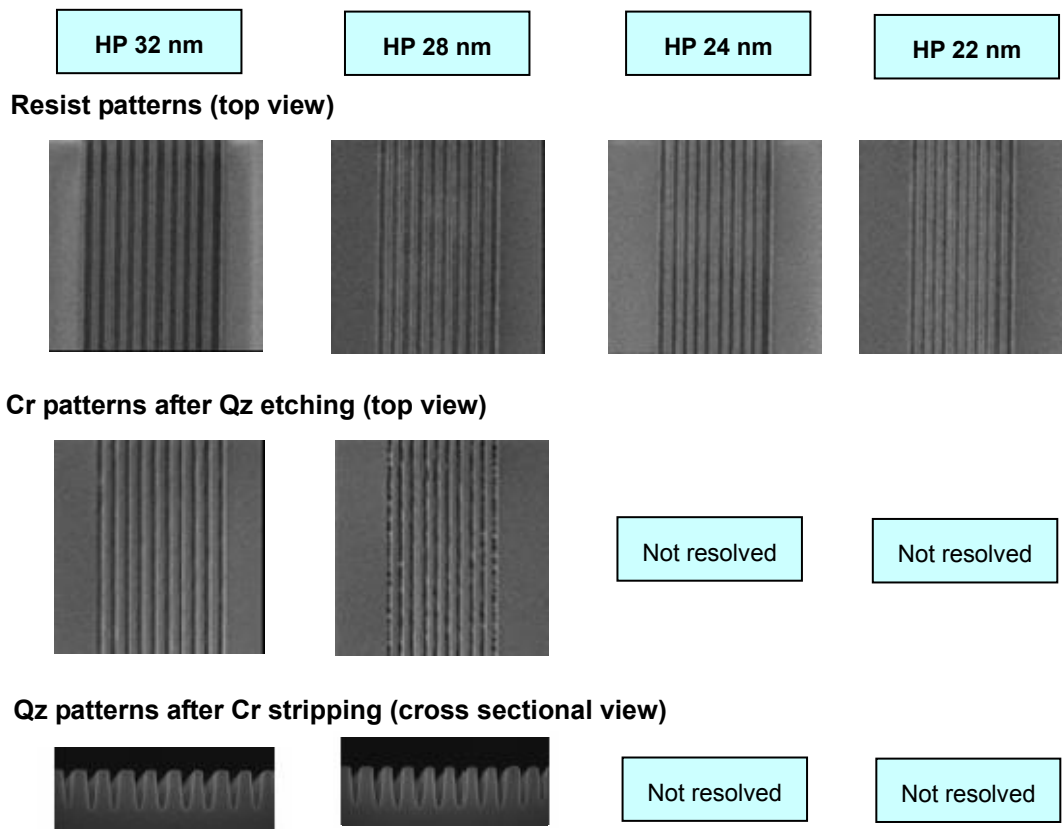


Fig. 3. Resolution of previous work

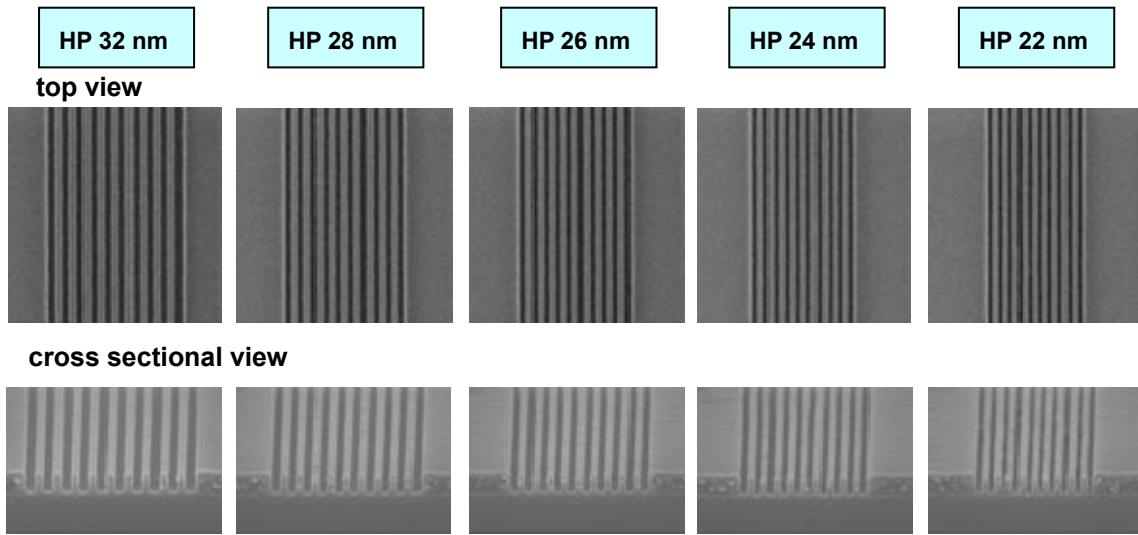


Fig. 4. Resist patterns of condition A

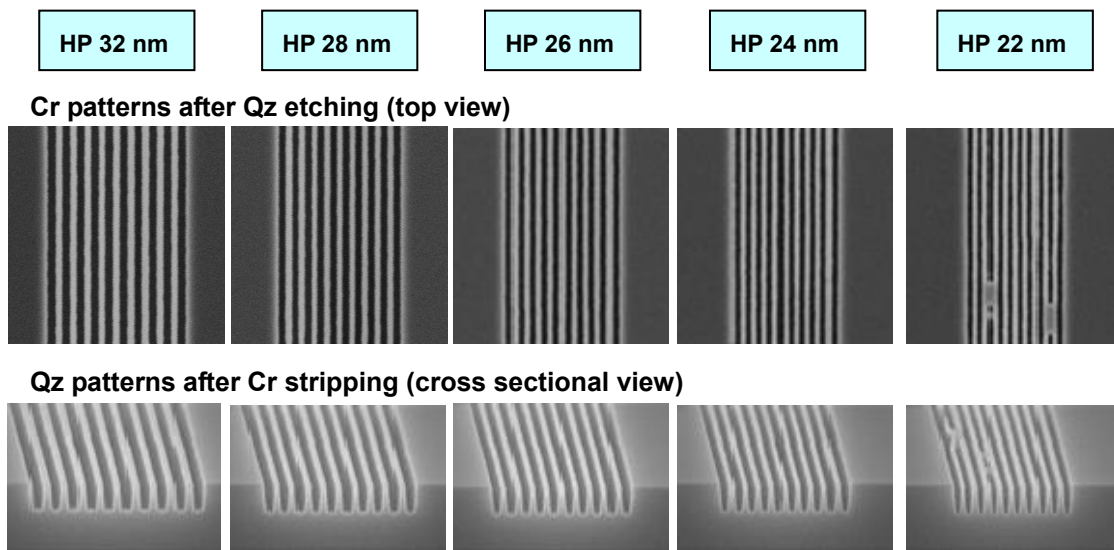


Fig. 5. Qz patterns of condition A

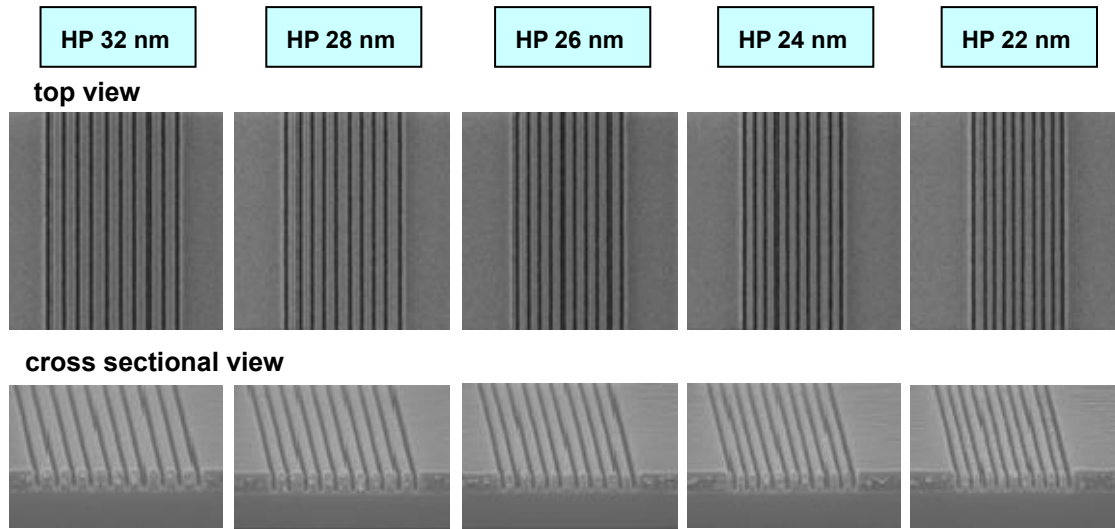


Fig. 6. Resist patterns of condition B

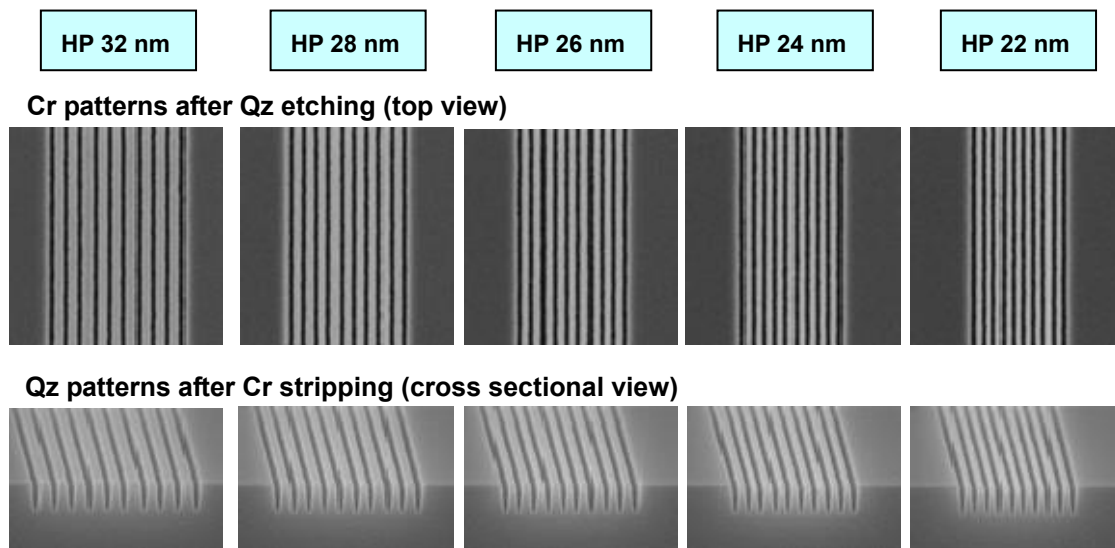


Fig. 7. Qz patterns of condition B

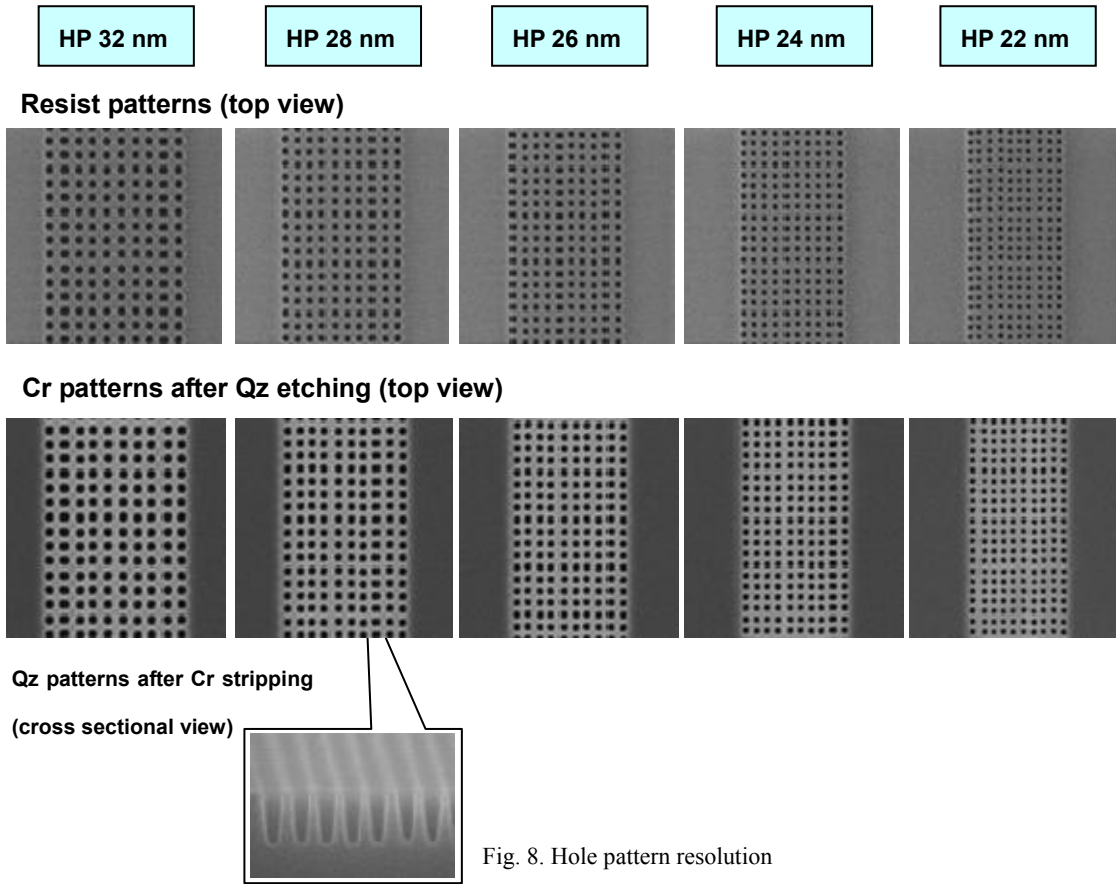


Fig. 8. Hole pattern resolution

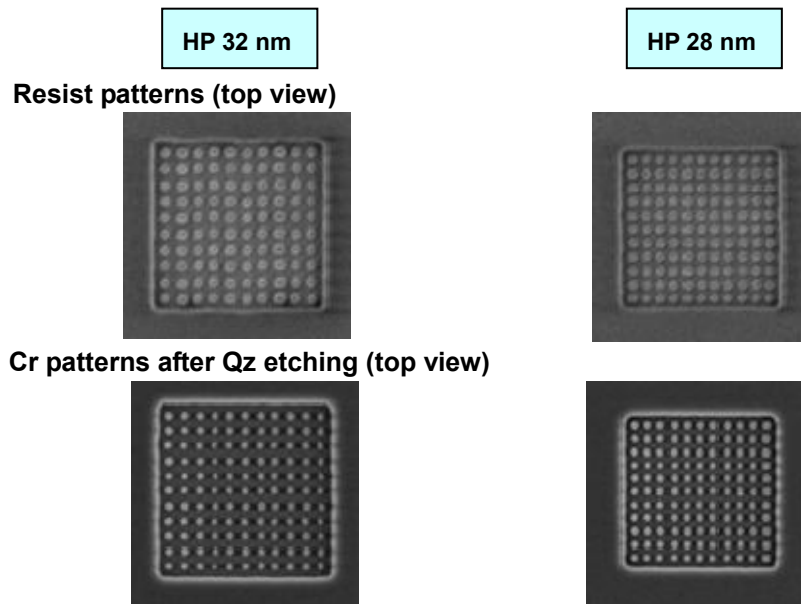


Fig. 9. Dot pattern resolution

Area 35mm (6X6)

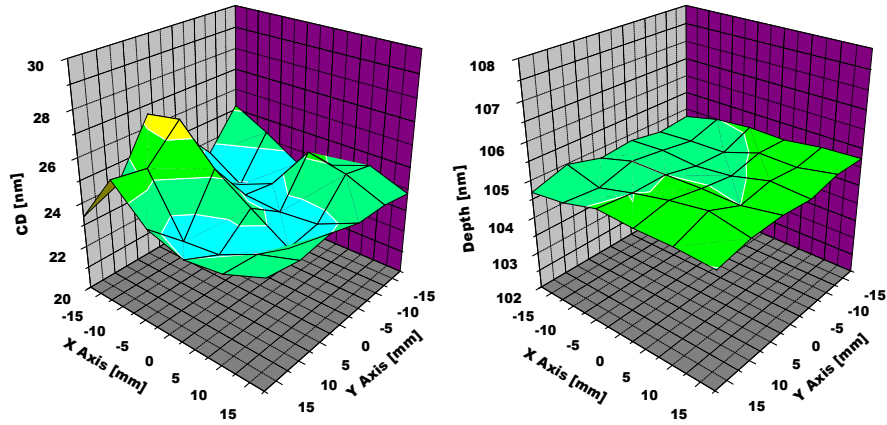


Fig. 10. CD uniformity and Qz depth uniformity

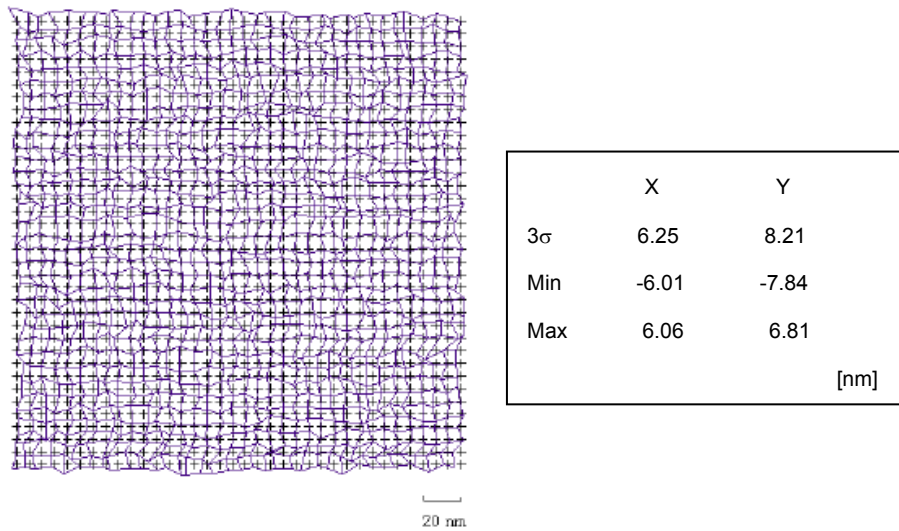


Fig. 11. CD uniformity and Qz depth uniformity

3-Dimensional bridged structures by thermal-UV imprint using a novel mask

*Keisuke Okuda, Hiroaki Kawata and Yoshihiko Hirai**
Graduate School of Engineering, Osaka Prefecture University
1-1, Gakuen-cho, Naka-ku, Sakai, 599-8531, Osaka, Japan
*E-mail:hirai@pe.osakafu-u.ac.jp

1. Introduction

Nano imprint lithography (NIL) is expected to realize low cost fabrication of fine patterns. Besides its high resolution, the major advantage is the applicability to a wide range of structure sizes in both, lateral and depth dimensions, as demonstrated by fabrication of mixed structures (micro and nano dimensions) with the newly proposed hybrid nanoimprint [1].

In this work, we report the first time about a single step procedure to fabricate 3-dimensional bridged structures by use of a novel type of mask similar to the one used in a hybrid nanoimprint process.

2. Bridged pattern transfer by imprint using a novel mask

2.1 Architecture of the novel mask

Figure 1 a) shows the schematic diagram of the novel mask for bridge fabrication. On the surface of a conventional photo mask, there are fine grating structures, where Cr is deposited on the bottom and on the top of the nano pattern as well. This area of the stamp is suitable for preparation of bridge structures

2.2 Process flow

Figure 1 b-d) shows the process flow of the bridge fabrication using the novel mask. First, a thick UV resist is prepared on a substrate and the mask is pressed into the resist in a thermal imprint at a temperature above the glass transition of the material (Fig.1-b), followed by cooldown. Next, UV light is irradiated at room temperature through the mask as shown in Fig. 1-c). During exposure the UV light is blocked below micron sized Cr structures, but only scattered by the Cr nano patterns (see Fig. 2). As a result, the surface region of the resist directly below the Cr- treated nano structures is slightly exposed by UV as demonstrated in Fig.2. After removing the mask, the resist is developed in a conventional way as shown in Fig.1-d). As a result, only the resist below the exposed surface region is removed by development and a bridged structure is fabricated.

2. 3 Experimental results

Figure 3 shows the experimental result. A 3-dimensional bridged structure having over 50 μm in height and around 30-50 μm in length is successfully fabricated using the novel UV mask. This method is extremely cost effective to fabricate 3-dimensional bridged structures without making use of any sacrificial layer or a multi-layer technique.

References

- 1) K.Okuda, et al.: *abstract of 2007 EMLC* (Grenoble, 2007)

*CV of the presenting author: Yoshihiko Hirai is graduated from Osaka Prefecture University in 1980. He received MS and PhD degrees in 1980 and 1995, respectively. In 1980, he joined Matsushita Electric Industrial Co. In 2004, he became a professor at Osaka Prefecture University. His research interest is nanoimprint lithography and fabrication of nano-patterns.

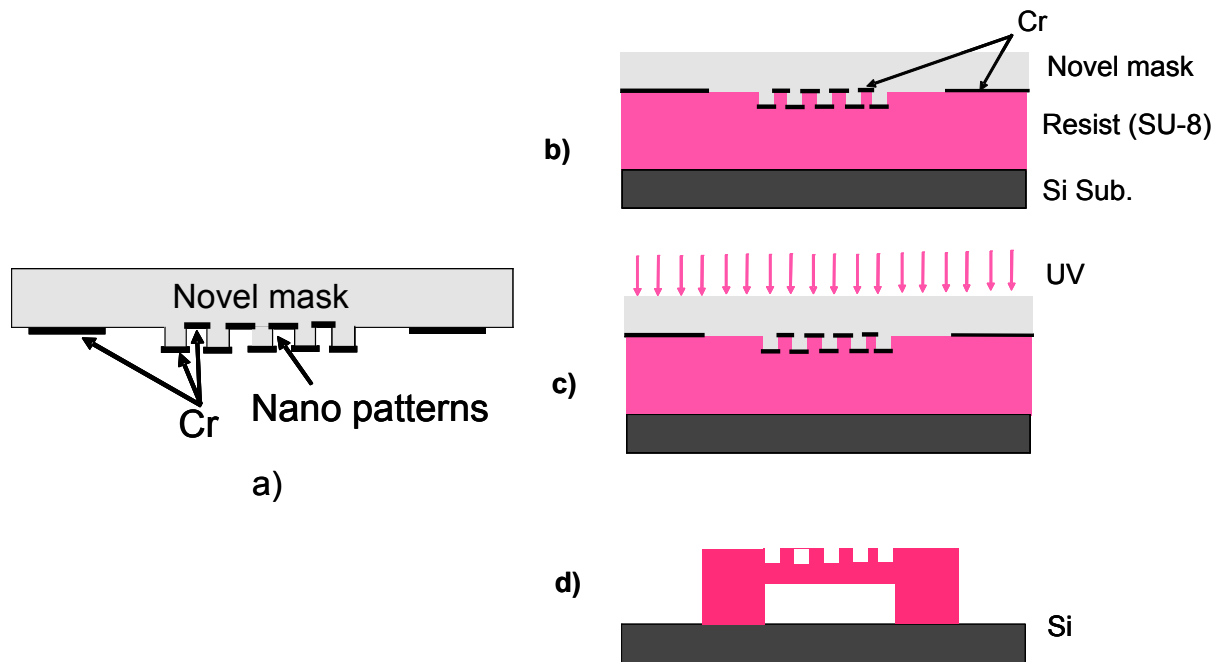


Fig. 1. Schematic diagram of the process flow for preparation of bridged structures by UV imprint

a) Novel UV mask having nano sutures with Cr

b) Thermal imprint

c) UV exposure

d) Resist development

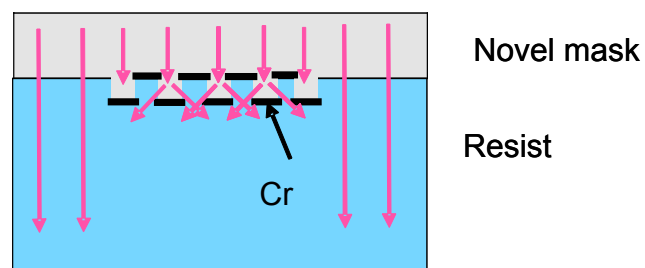


Fig. 2. Schematic diagram of the exposure by diffraction / scattering.

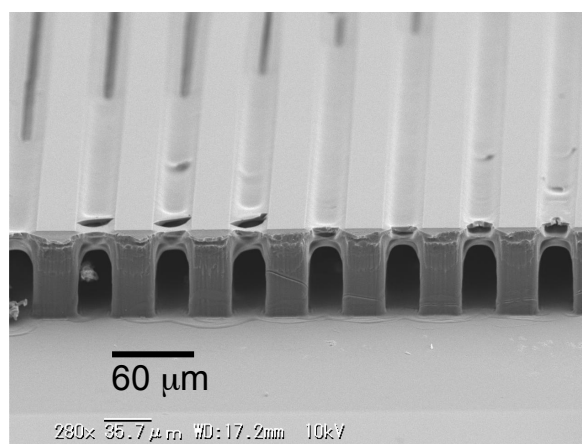


Fig. 3. Bridged SU-8 structures prepared in a single step by thermal-UV imprint using the novel mask.

Polarization-induced astigmatism caused by topographic masks

Johannes Ruoff^a, Jens Timo Neumann^a, Emil Schmitt-Weaver^b, Eelco van Setten^c, Nicolas le Masson^c, Chris Progler^d, Bernd Geh^{a,e}

^aCarl Zeiss SMT AG, D-73446 Oberkochen, Germany

^bASML US, Inc., DE Adv. Lithogr. Appl. Research, 25 Corporate Circle, Albany, NY

^cASML Netherlands B. V. de Run 6501, 5504 DR Veldhoven, The Netherlands

^dPhotronics Inc., 601 Millennium Drive, Allen, Texas

^eASML US, Inc., 8555 S. River Parkway, Tempe, AZ

ABSTRACT

With the continuous shrink of feature sizes the pitch of the mask comes closer to the wave length of light. It has been recognized that in this case polarization effects of the mask become much more pronounced and deviations in the diffraction efficiencies from the well known Kirchhoff approach can no longer be neglected. It is not only the diffraction efficiencies that become polarization dependent, also the phases of the diffracted orders tend to deviate from Kirchhoff theory when calculated rigorously. This also happens for large structures, where these phase deviations can mimic polarization dependent wave front aberrations, which in the case of polarized illumination can lead to non-negligible focus shifts that depend on the orientation and the features size themselves. This orientation dependence results in a polarization induced astigmatism offset, which can be of the same order of magnitude or even larger as polarization effects stemming from the lens itself. Hence, for correctly predicting polarization induced astigmatism offsets, one has to both consider lens and mask effects at the same time. In this paper we present a comprehensive study of polarized induced phase effects of topographic masks and develop a simple theoretical model that accurately describes the observed effects.

Keywords: Topographic mask, Polarization, Jones pupils, Wave Front Aberrations

1. INTRODUCTION

With the continuing demand to reduce cost in chip production, one of the paradigms within the semiconductor industry is the further shrinking of the volume of a single logic or memory unit in order to increase the number of memory units per wafer or the number of dies. For the current 65nm node the smallest pitches are already approaching 120nm, which means that the corresponding pitch on the mask for a 4X reduction system is of the order of two times the wavelength. For the future nodes to come the mask pitch can even become smaller than 1.5 times the wavelength of light. It has been recognized early on that with the mask pitch approaching the range of the wavelength, polarization effects become important, and the diffraction amplitudes can no longer be accurately predicted using the well established Kirchhoff approximation, which was used to compute the diffraction amplitudes of binary, attenuated or phase shifting masks. Instead, the full set of Maxwell's equations, which take care of the polarization and the finite thickness of the mask, have to be solved in order to correctly predict the diffraction spectrum of the mask. At present, all established litho simulation tools offer the possibility to rigorously compute the mask spectrum using various Maxwell solvers. Among the widespread methods are the Finite Difference Time Domain (FDTD), which solves the time dependent Maxwell equations, or the Rigorous Coupled Wave Analysis (RCWA), which solve Maxwell's equations in Fourier Space. The RCWA is particularly suited for periodic patterns, such as lines and spaces, but also contact holes array, whereas the FDTD in principle can handle any kind of mask patterns, although it might be very time and memory consuming.

There have been numerous studies on topographic mask effects, which dealt with the influence of mask imperfection, such as side wall angles, the influence of the mask material – which in case of chrome is, of course,

not perfectly absorbing –, and many more.^{1,2} Most of these studies were performed for the smallest critical dimensions, since here deviations from the Kirchhoff approximation are the most severe, which can show up, for instance, as strongly deformed Bossung curves.³ In this paper, the focus is on large structures and it is shown that even here, one has to expect significant deviations from Kirchhoff theory and polarization dependent effects do occur. These effects are hidden for unpolarized illumination settings, but have a nonnegligible effect, when polarized light is used. As will be shown, these electromagnetic effects mainly affect the phases of the diffraction orders in such a way that for a given polarization state, the best focus of a vertical and horizontal line will generally differ, and under particular circumstances by a considerable amount. Even though the effects are small, they are inherent to topographic masks, and they contribute to or may even dominate the overall retardation effects, such as mask blank birefringence, lens birefringence, stemming from coatings and material birefringence.

The paper is organized as follows: In Section 2, we set the stage using a simplified, but possibly realistic example. Section 3 revisits some results from Kirchhoff theory and in Section 4 we present a comprehensive study of the 3D phase effects and their dependence on various parameters. In Section 5 we devise a simple modification of the Kirchhoff theory, which leads to an accurate description of the observed mask effects. Experimental results obtained on various different scanner systems are presented in Section 6 and conclusions are drawn in Section 7.

2. ILLUSTRATING EXAMPLE

As an illustrating example, we consider a case, where we want to print a layer consisting of a dense core structure and a periphery containing much larger horizontal and vertical semidense and isolated lines.

To be more specific, we choose the core structure to consist of dense vertical lines with 60nm CD and 120nm pitch. For a dry scanner system with $NA = 0.93$, this amounts to $k_1 = 0.29$. For illumination a horizontal y-polarized 40 degree dipole with $\sigma_i = 0.6$ and $\sigma_o = 0.95$ is chosen. In the periphery the isolated lines are required to print at 200nm. For the sake of simplicity, in the following we will only consider the image in resist, instead of performing a full fledged resist simulation, since for our purpose this will lead to the same qualitative results.

Neglecting any polarization influences other than the vectorial effects in the resist, we fix the intensity threshold such that the core structures print on size. Based on this threshold the appropriate biases for the 200nm isolated lines are determined by requiring them to print on size. For the vertical line, we find that the required CD on mask side is 254nm, for the horizontal line it is 182nm.

In order to have a more realistic description, we now include the polarization effects coming from the mask and also the retardation effect of the projection lens, which is due to antireflection coatings and material birefringence, and which is conveniently described by a Jones pupil.⁴

For the 60nm line, the main effect of using 3D and Jones pupil is an increase of the CD in the resist image, which comes from the fact that the rigorously computed diffraction efficiencies are somewhat lower than the ones stemming from the Kirchhoff approximation. This can be readily compensated for by lowering the intensity threshold, which amounts to increasing the exposure dose.

What do we expect to see for the isolated lines? Since they are large structures, we do expect that the diffraction efficiencies should be well described by the Kirchhoff approximation, which means that dose effects should be almost negligible. For polarized imaging, however, the presence of birefringence in the lens translates into aberrations of the polarized wave front. As retardation effects due to coatings and stress birefringence are predominantly rotationally symmetric, they translate into astigmatic aberrations in the Jones pupil. Therefore we would expect the horizontal and vertical lines to have different locations of best focus.

And this is what the simulation actually show. In Figure 1a, the CDs of both the horizontal and vertical lines are shown as a function of defocus. Since best focus (BF) is defined as the point where the CD exhibits an extremum, in this case, a maximum, we see that there is a BF difference of about 90nm, which seems to be a relatively large value, and which could lead to the conclusion that there is a rather strong birefringence present in the lens. As we are only simulating, we are in a position, where we can just switch off the lens birefringence and see how much focus shift will still remain. By doing so, we obtain the results shown in Figure 1b, which still

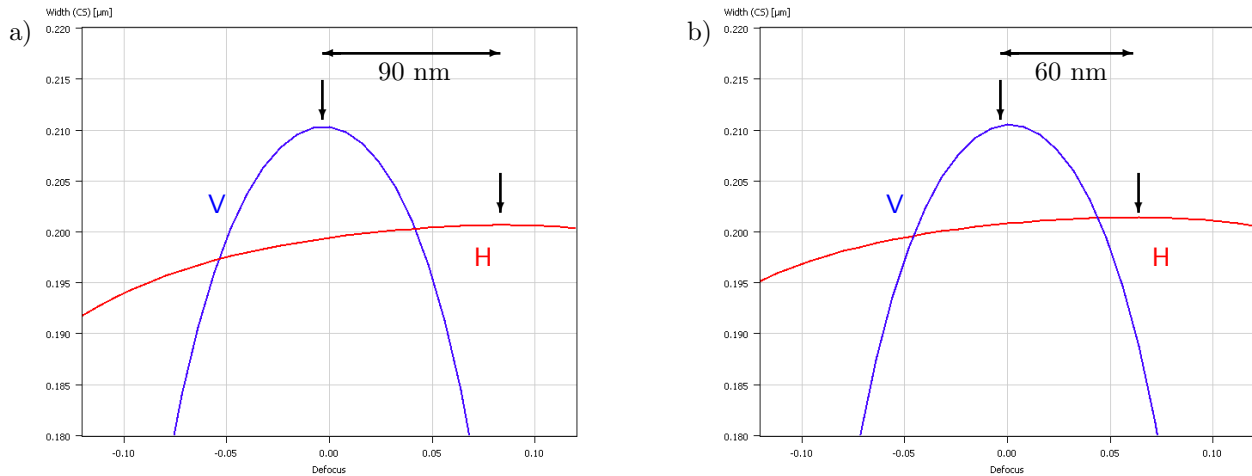


Figure 1. CD as function of defocus for horizontal (H) and vertical (V) iso lines. a) With 3D mask effects and Jones pupil: BF difference about 90nm. b) 3D mask effects only: BF difference about 60nm.

shows 60nm BF difference! This means that only one third of the observed BF difference is due to the lens and two thirds have to be attributed to the mask alone.

Before we continue exploring which effects in the mask are responsible for this focus shift, we should note that although 60nm may look large, the influence on the process window is rather small. This is because the horizontal line, which is much stronger affected than the vertical line also has a much broader depth of focus, which allows for larger BF shift without deteriorating the process window. The BF of the vertical line, which exhibits a much smaller DOF almost remains unaffected by either the Jones pupil or the 3D mask effect. Nevertheless, with the CD tolerances becoming ever tighter, these effects eventually have to be taken into account.

In order to study the mask effects in a more systematic way, we shall abandon the dipole illumination, which only served for setting up a more realistic scenario. However, due its asymmetric shape, it introduces an asymmetry between the H and V lines, leading to different biases and different depths of focus. For the following discussion, we therefore switch to a conventional low sigma illumination setting, restoring the symmetry between H and V lines. The only asymmetry then comes from the chosen linear polarization of the illumination.

3. KIRCHHOFF THEORY

Before presenting the rigorous simulation results, we shall derive some useful analytic results for binary masks using the Kirchhoff approximation, where the mask is considered to be infinitely thin. In this case, the mask can be described by a complex amplitude transfer function, and for binary or attenuated phase shift masks the diffraction spectrum can be computed analytically. For the sake of simplicity, we restrict ourselves to binary masks.

In scalar Kirchhoff theory, the diffraction spectrum of a periodic mask with complex amplitude transfer function $T(x)$ can be computed through discrete Fourier transformation over one period of the mask. Thus the m^{th} diffraction coefficient b_m can be obtained by

$$b_m = \int_0^1 T(x)e^{-2\pi imx} dx . \quad (1)$$

Herein the period has been normalized to one. For a binary mask $T(x)$ is simply given by

$$T(x) = \begin{cases} 0, & 0 < x \leq f \\ 1, & f < x \leq 1 \end{cases} , \quad (2)$$

where f is the fillfactor defined as the ratio of linewidth viz. CD and pitch:

$$f = \frac{\text{CD}}{\text{pitch}} . \quad (3)$$

Inserting $T(x)$ into (1) yields

$$b_m = (1 - f) e^{im\pi(1+f)} \text{sinc}(m(1 - f)) , \quad (4)$$

with the sinc-function defined as

$$\text{sinc}(x) := \frac{\sin(\pi x)}{\pi x} . \quad (5)$$

The diffraction efficiency η_m of the m^{th} order is the squared modulus of the complex amplitude

$$\eta_m = |b_m|^2 = (1 - f)^2 \text{sinc}^2(m(1 - f)) . \quad (6)$$

The diffraction angle of the m^{th} transmitted order can be inferred from the well known grating equation

$$n_{out} \sin \theta_{out}^m = n_{in} \sin \theta_{in} + \frac{m\lambda}{g} , \quad (7)$$

where $n_{in/out}$ are the refractive indices of the surrounding media. We denote by g the period of the mask, which corresponds to a pitch on wafer level, which is reduced by the reduction factor R of the lens, with $R = 4$ for current high end projection lenses. For normal incidence it is $\theta_{in} = 0$ and together with $n_{out} = 1$ we obtain

$$\sin \theta_{out}^m = \frac{m\lambda}{g} . \quad (8)$$

Introducing pupil coordinates σ by

$$\sigma = \frac{R}{\text{NA}} \sin \theta_{out}^m , \quad (9)$$

we can represent the diffraction order m by a pupil position σ :

$$m = \frac{g \text{NA}}{R\lambda} \sigma = \frac{\text{pitch NA}}{\lambda} \sigma . \quad (10)$$

Using the relation, we can express the diffraction efficiencies (6) as a function of the pupil coordinate sigma, which will be used for the graphical representations. The inverse relation is given by

$$\sigma = \frac{m\lambda}{\text{pitch NA}} . \quad (11)$$

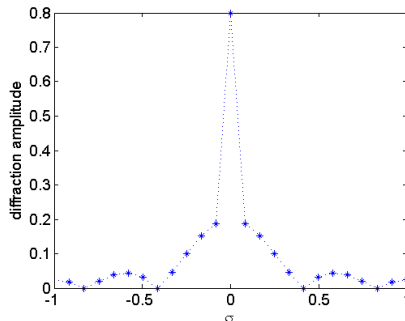


Figure 2. Scalar diffraction amplitude of a binary 500nm/2500nm Kirchhoff mask

Throughout the following discussion we will use $\text{NA} = 0.93$ and $\lambda = 193 \text{ nm}$. Figure 2 shows the magnitude of the scalar diffraction amplitudes of a 500nm/2500nm binary line according to formula (1). We did not plot the efficiencies, since the difference between the zeroth and the other orders would be too big to produce a decent graph. Apart from the dominating zeroth order, the diffraction orders follow a periodic pattern, decreasing in amplitude according to the sinc-function. It is obvious that most of the diffracted intensity is located between the first zeros at the left and right of the zeroth diffraction order. The location of the zero can be easily computed, if we assume that the pitch is an integer multiple of the CD. Let this factor be denoted by p , it is then straightforward to

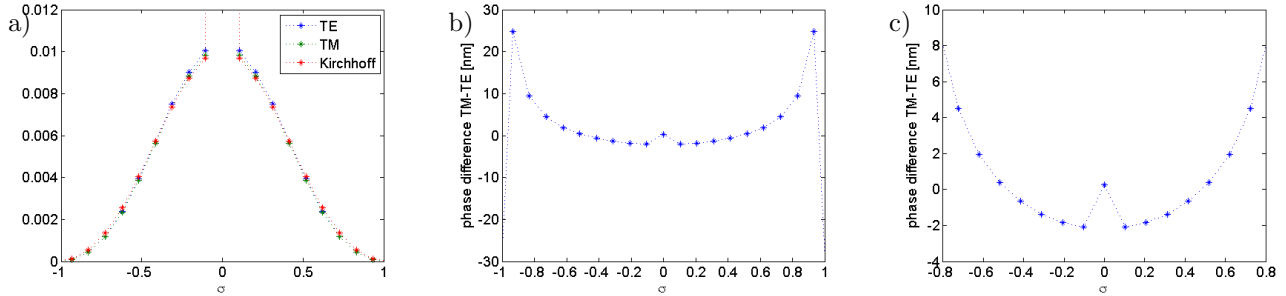


Figure 3. a) Comparison of the diffraction efficiencies of a scalar Kirchoff mask and rigorous Chrome mask for TE and TM polarization. b) Phase differences between TE and TM polarization due to electromagnetic effects at the mask. c) Same as b), but with σ restricted to $[-0.8, 0.8]$.

show that the p^{th} diffraction order always lies on the first zero: From equation (6) we find that the diffraction efficiency becomes zero whenever

$$m(1 - f) = n, \quad n \in N. \quad (12)$$

Since we assumed that pitch = p CD, the fillfactor f can be written as

$$f = \frac{1}{p} \quad (13)$$

and condition (12) becomes

$$m = \frac{np}{p - 1}. \quad (14)$$

Clearly, for $n = p - 1$, it is $m = p$, and it is easy to show that this is the smallest diffraction order m , for which condition (14) holds. The corresponding pupil coordinate σ_0 can be obtained from (11):

$$\sigma_0 = \frac{\lambda}{\text{CD NA}}. \quad (15)$$

Note that σ_0 is independent of pitch. This means that for a pitch of p -times the CD, the p -th diffraction order will have zero efficiency, and for any p it will always be found at the same pupil coordinate σ_0 . In case that the pitch is not an integer multiple of the CD, there is no diffraction order which has exactly zero efficiency, but nevertheless the orders which lay close to σ_0 will have very small efficiencies.

4. RIGOROUS SIMULATIONS

Having established that the location of the first zero is independent of the pitch, we can now move on to assess the influence of the electromagnetic mask effects on the diffraction coefficients. The simulations were performed using the Rigorous Coupled Wave Method with a large number of Fourier modes (up to several hundreds for the large pitches) to make sure that the results were well converging. As these phase effects are rather small, the convergence is rather slow, and therefore this large number of Fourier modes was necessary for accurate results.

In Figure 3a, we compare the diffraction efficiency of the scalar Kirchoff mask with the efficiencies obtained by the RCWA Maxwell solver for a 200nm isolated chrome line for TE and TM polarization. The differences between the rigorously computed values and the ones obtained by formula (6) are very small, indicating that for the efficiencies the Kirchoff theory provides very accurate results.

Let us turn to the phases. As the absolute values of the phases are not of interest, we plot in Figures 3b and 3c the phase differences between TM and TE polarization. In Figure 3b the phase difference is plotted for the complete pupil range. Obviously, close to pupil edges, the phase differences become very large when approaching

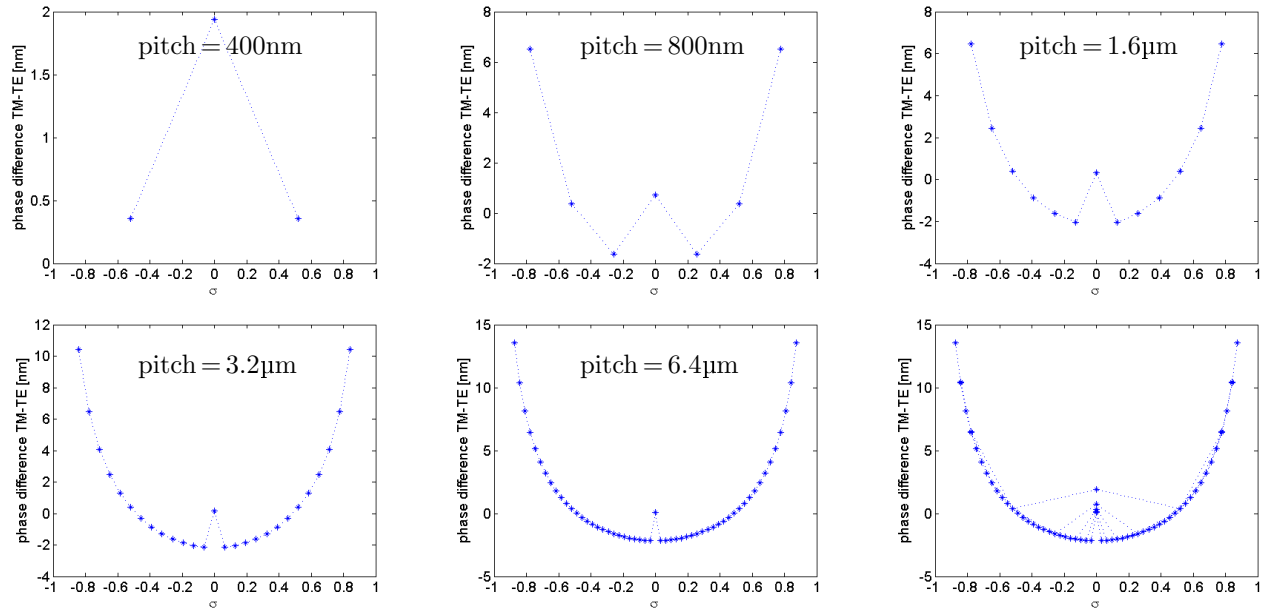


Figure 4. Phase differences between TE and TM for a 200nm binary line for different pitches. The asterisks indicate the positions of the diffraction orders. In the last panel, all graphs are drawn on top of each other.

$\sigma = 1$. At the same time, however, the diffraction efficiencies go to zero, since for the chosen values ($CD = 200\text{nm}$, $NA = 0.93$, $\lambda = 193\text{nm}$), it is $\sigma_0 = 1.04$. This means that the corresponding diffraction orders do not significantly contribute to the image formation. Therefore the important part to look at is in a sigma range of about $\pm 0.8\sigma_0$, since only here the diffraction efficiencies are large enough to account for imaging. The phase differences between TE and TM polarization restricted to this interval are shown in Figure 3c. If it were not for the zeroth diffraction order, which shows a much larger phase difference than its neighboring higher orders, the curve could be accurately fitted by a polynomial with even orders only.

Such a polynomial can also be written in terms of the radial Zernike polynomials Z_1, Z_4, Z_9, Z_{16} , etc. with Z_4 describing defocus and Z_9, Z_{16} , etc. the higher order spherical aberrations. If we now consider the TE polarized case as a reference, this means that the TM polarized case will experience a phase shift or wave aberration with respect to the TE case, which contains a certain amount of defocus and spherical aberration. Hence, the images of both the TE and TM polarized cases will have different focus positions. Moreover, the spherical aberration should lead to a tilting of the Bossung curves, which can also be observed. From the amount of Z_4 that can be deduced from the polynomial fit, one should immediately be capable to predict the corresponding focus difference. However, due to the presence of the zeroth diffraction order, where the phase difference deviates from the smooth curve, this analysis is slightly more complicated, and especially in the intermediate region, where the pitch is only a few times the CD, the difference between the first order and its neighbors is quite pronounced, and therefore the focus behavior cannot be deduced by the amount of Z_4 , which would be obtained from the polynomial fit. Nevertheless, as will be corroborated by simulations and experiments, it is this phase difference between TE and TM, which is responsible for the occurrence of best focus differences with polarized illumination.

In the following we will investigate the dependence of these phase effects on pitch, CD, mask thickness and angle of incidence.

4.1 Pitch dependence

Figure 4 shows the TM-TE phase differences of a 200nm Cr-line for various pitches ranging from 400 nm through 1.6 μm . For a 400 nm pitch, only three diffraction orders fall into the lens pupil. For 800 nm pitch, we have seven orders, and for larger pitches the number of diffraction orders increases accordingly. On the lower right panel, all curves are plotted on top of each other and it becomes apparent that they all lie on a single universal

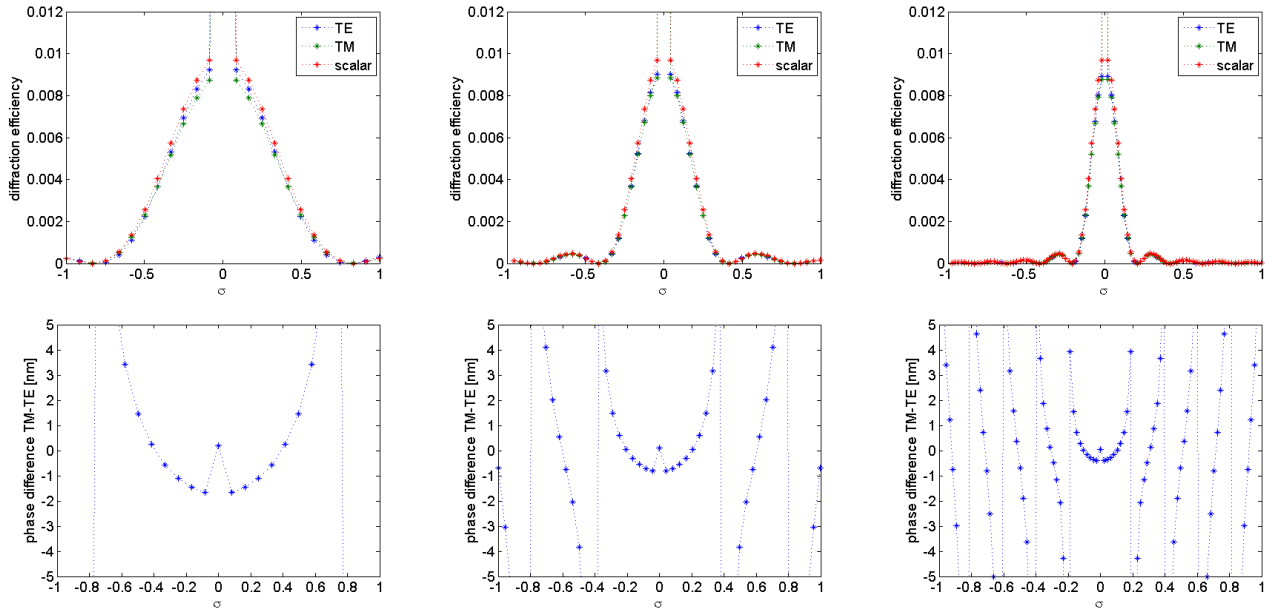


Figure 5. Diffraction efficiencies (upper row) and phase differences between TE and TM (lower row) for different CD values (250, 500, 1000nm). For each panel, pitch = $10 \times \text{CD}$.

curve, independent of pitch! Only the zeroth order is an exception since this is the only order where the phase difference actually does depend on pitch.

4.2 CD dependence

Figure 5 shows both the diffraction efficiencies and the phase differences as a function of CD over the complete pupil range. The pitch has been set to 10 times the CD. Increasing the CD results in squeezing the diffraction spectrum such that the light get more and more concentrated around the pupil center. Note the phase singularities at the points where the diffraction efficiency goes to zero. Since in all cases, most of the light is contained between the first zeros around the center, it is always this area where the phase differences are relevant.

To make this area independent of the CD, we can scale the σ -coordinate by σ_0 . So instead of using σ we use σ/σ_0 to plot the phase differences. In Figure 6a the effect of this scaling is shown, where we have plotted in a single graph the phase differences with scaled pupil coordinates for 250nm, 500nm and 1000nm iso lines. As can be seen, the phase effects weaken with increasing CD. If we quantify the strength of the phase difference by its PV-value inside this range, we can plot it as a function of CD, which is depicted in 6b. As it turns out, the decrease of the PV-value is proportional to $1/\text{CD}$.

4.3 Thickness and material dependence

The dependence on line thickness d and material is depicted in Figure 6c, where the PV is plotted for both a chrome and a MoSi 200nm line as function of thickness. For both materials in the range between 10nm and 100nm an almost linear dependence on thickness can be observed, with the effect being much stronger for chrome than for MoSi.

4.4 Dependence on angle of incidence

The dependence on the angle of incidence is rather weak as can be inferred from Figure 7. In this graph, the phase differences for normal incidence and incidence angles corresponding to $\sigma_{\pm} = \pm 1.35/2$ have been plotted. Even for the largest angle of incidence which would occur for a state of the art hyper NA immersion scanner, only a small tilt due to oblique incidence is discernible.

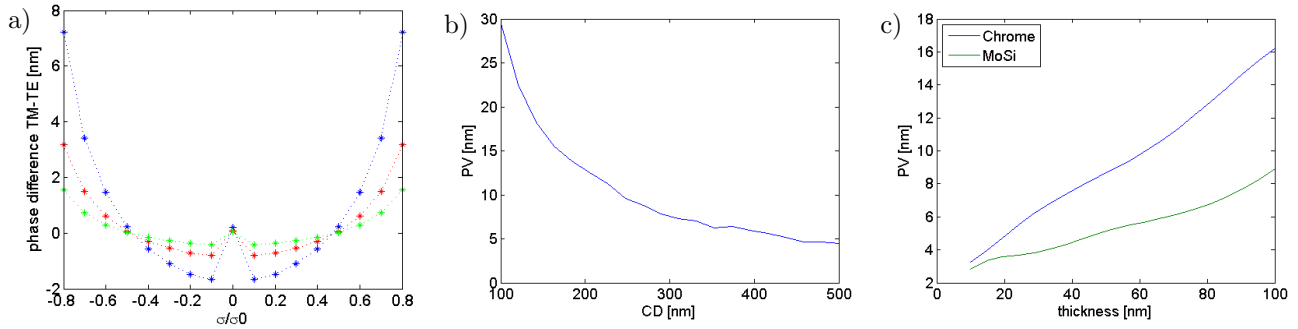


Figure 6. a) Phase differences between TE and TM for 250nm, 500nm and 1000nm Cr line using the scaled pupil coordinate. b) PV value as function of CD for a Cr line. c) PV dependence on thickness for Cr and MoSi.

Summarizing the so far obtained results, we can conclude that the strength of the phase effect is proportional to the line thickness d , independent of pitch, and inversely proportional to the line width. This can be subsumed in the following simple formula:

$$\text{strength} = M \frac{d}{\text{CD}}, \quad (16)$$

where M is a material dependent proportionality factor. By strength, we mean for instance the PV level for the scaled pupil coordinates.

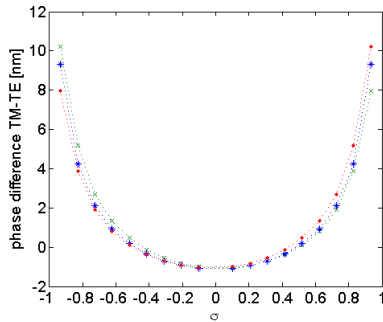


Figure 7. Dependence of the phase difference on the angle of incidence.

difference in the boundary conditions, it is then obvious that we can expect a linear dependence on the line thickness since by making the line thicker, the region where the boundary conditions differ for TE and TM also grows.

These results suggest that it is mainly the vertical slopes of the lines that are responsible for the observed phase differences. This can also be seen by looking at the boundary condition for the electromagnetic fields, which follow from Maxwell's equations. If we consider normal incidence, then for large structures the propagation directions of those transmitted and reflected diffraction orders which carry the substantial amount of energy will also be close to the normal, i.e. the diffraction angles are very small. In this case, the boundary conditions for the horizontal boundaries, i.e. the top and bottom of the line and the bottom of the substrate, are identical for TE and TM polarization as in both cases the electric field is parallel to the boundary. However, at the vertical walls the boundary conditions differ for TE and TM. For TE polarization the electric field component is parallel to the wall and, therefore, continuous. In the TM case, however, the electric field is perpendicular to the wall and must be discontinuous. Assuming that the observed phase effects are due to this

5. DERIVATION OF A SIMPLE THEORETICAL KIRCHHOFF MODEL

To further corroborate our statement that the phase differences are purely caused by the edge effects at the vertical walls, we propose a simple modification of the Kirchhoff theory that, as we shall show, gives remarkable agreement with the observed phase effects.

Let us suppose that the edge effects can be mimicked in scalar theory by adding to the binary transmission function $T(x)$ from Eq.(2) two δ -functions with a certain amplitude A and phase ϕ , representing perturbation coming from the edges. The modified transmission function thus reads

$$T_{\text{pert}}(x) = T(x) + Ae^{i\phi}\delta(x - 0) + Ae^{i\phi}\delta(x - f). \quad (17)$$

The amplitude A and phase ϕ , of course, depend on the polarization. Inserting the perturbed transfer function (17) into (1) and performing the integral yields

$$b_m = e^{im\pi f} \left((1-f) e^{im\pi} \text{sinc}(m(1-f)) + 2Ae^{i\phi} \cos(\pi m f) \right). \quad (18)$$

In order to further simplify the above equation, we assume that $m \neq 0$. The case $m = 0$ will be dealt with subsequently. For $m \neq 0$ it is straightforward to show that

$$(1-f) e^{im\pi} \text{sinc}(m(1-f)) = -f \text{sinc}(mf), \quad (19)$$

and after discarding the global phase factor $\exp(im\pi f)$, we find for the phase Φ_m of the m^{th} diffraction order

$$\begin{aligned} \tan \Phi_m &= \frac{\text{Im } b_m}{\text{Re } b_m} = \frac{2A \sin \phi \cos(\pi m f)}{-f \text{sinc}(mf) + 2A \cos \phi \cos(\pi m f)} \\ &\approx -\frac{2\pi m A \sin \phi \cos(\pi m f)}{\sin(\pi m f)} \\ &= -2\pi m A \sin \phi \cot(\pi m f). \end{aligned} \quad (20)$$

Instead of using the diffraction order m , let us switch to the pupil coordinate σ through

$$m = \frac{\text{pitch NA}}{\lambda} \sigma. \quad (21)$$

By virtue of (15) and (3) it is

$$mf = \frac{\sigma}{\sigma_0}, \quad (22)$$

and we can further simplify (20) assuming that Φ_m is small enough for $\tan \Phi_m \approx \Phi_m$ to hold:

$$\Phi_m \approx -2\pi \frac{A\sigma}{f\sigma_0} \sin \phi \cot\left(\frac{\pi\sigma}{\sigma_0}\right). \quad (23)$$

Note that we keep the index m at the Φ_m to stress that Φ_m is still a discrete quantity, although as a function of the pupil coordinate σ it looks continuous.

Let us now turn our attention towards the zeroth order $m = 0$. In this case, Equation(18) becomes

$$b_0 = 1 - f + 2Ae^{i\phi}. \quad (24)$$

with its phase

$$\tan \Phi_0 = \frac{2A \sin \phi}{1 - f + 2A \cos \phi} \quad (25)$$

or for small amplitude A

$$\Phi_0 \approx \frac{2A \sin \phi}{1 - f}. \quad (26)$$

In the following, we always will have to distinguish between the cases $m \neq 0$ and $m = 0$. The latter case will always be indicated by a zero subscript, otherwise $m \neq 0$ is assumed.

In principle, we would need four parameters $A_{\text{TM}}, A_{\text{TE}}, \phi_{\text{TM}}, \phi_{\text{TE}}$, to describe both the perturbations for TE and TM polarization. However, the phase difference $\Delta\Phi_m = \Phi_m^{\text{TM}} - \Phi_m^{\text{TE}}$ can be described by a single effective parameter A_{eff} , since it is

$$\begin{aligned} \Delta\Phi_m &= -2\pi \frac{\sigma}{f\sigma_0} (A_{\text{TM}} \sin \phi_{\text{TM}} - A_{\text{TE}} \sin \phi_{\text{TE}}) \cot\left(\frac{\pi\sigma}{\sigma_0}\right) \\ &= A_{\text{eff}} \frac{\pi\sigma}{f\sigma_0} \cot\left(\frac{\pi\sigma}{\sigma_0}\right) \end{aligned} \quad (27)$$

with

$$A_{\text{eff}} = 2 (A_{\text{TE}} \sin \phi_{\text{TE}} - A_{\text{TM}} \sin \phi_{\text{TM}}) . \quad (28)$$

Before discussing the implications of this formula, we shortly turn to the diffraction efficiencies. The difference $\Delta\eta = \eta_m^{\text{TM}} - \eta_m^{\text{TE}}$ can be readily obtained from the diffraction coefficients (18):

$$\begin{aligned} \Delta\eta_m &= |b_m^{\text{TM}}|^2 - |b_m^{\text{TE}}|^2 \\ &= |f \text{sinc}(mf) - 2A_{\text{TM}} e^{i\phi_{\text{TM}}} \cos(\pi mf)|^2 - |f \text{sinc}(mf) - 2A_{\text{TE}} e^{i\phi_{\text{TE}}} \cos(\pi mf)|^2 \\ &\approx -2f (A_{\text{TM}} \cos \phi_{\text{TM}} - A_{\text{TE}} \cos \phi_{\text{TE}}) \text{sinc}(mf) \cos(\pi mf) \\ &= f B_{\text{eff}} \text{sinc}(mf) \cos(\pi mf) , \end{aligned} \quad (29)$$

with

$$B_{\text{eff}} = 2 (A_{\text{TE}} \cos \phi_{\text{TE}} - A_{\text{TM}} \cos \phi_{\text{TM}}) . \quad (30)$$

From a comparison of this formula with rigorous simulations for various CD and pitches, we found that $\Delta\eta_m \sim \text{CD}/\text{pitch}^2 = f^2/\text{CD}$. Since from Equation (29) it follows that $\Delta\eta_m \sim f B_{\text{eff}}$, we conclude that $B_{\text{eff}} \sim f/\text{CD}$. The same has to hold for A_{eff} , as well. Now, from Equation (27), we see that $\Delta\Phi_m \sim A_{\text{eff}}/f$, and it immediately follows that $\Delta\Phi_m$ only depends on $1/\text{CD}$, which is consistent with the numerical simulations of the previous section. Moreover, the rigorous simulations have shown that the strength of the phase effects depends linearly on the line thickness d . We can therefore introduce scaled effective amplitudes \tilde{A}_{eff} and \tilde{B}_{eff} via

$$A_{\text{eff}} = \tilde{A}_{\text{eff}} \frac{df}{\text{CD}} , \quad (31)$$

$$B_{\text{eff}} = \tilde{B}_{\text{eff}} \frac{df}{\text{CD}} , \quad (32)$$

and write the phase and efficiency differences as

$$\Delta\eta = \tilde{B}_{\text{eff}} \frac{df^2}{\text{CD}} \text{sinc}\left(\frac{\sigma}{\sigma_0}\right) \cos\left(\frac{\pi\sigma}{\sigma_0}\right) , \quad (33)$$

$$\Delta\Phi = \tilde{A}_{\text{eff}} \frac{d}{\text{CD}} \frac{\pi\sigma}{\sigma_0} \cot\left(\frac{\pi\sigma}{\sigma_0}\right) . \quad (34)$$

The coefficients \tilde{A}_{eff} and \tilde{B}_{eff} then only depend on the material of the line stack. This is perfectly consistent with our heuristic statement on the strength of the phase differences as given in (16), with the strength now represented by the effective amplitude \tilde{A}_{eff} . Note also that there is no pitch dependence for $\Delta\Phi$, which is consistent with the numerical results (cf. Figure 4).

So far, these results are only valid for $m \neq 0$. For $m = 0$, we find from Equation (26)

$$\Delta\Phi_0 = \frac{A_{\text{eff}}}{1-f} = \tilde{A}_{\text{eff}} \frac{f}{\text{CD}(1-f)} . \quad (35)$$

In contrast to the phase difference for $m \neq 0$, for $m = 0$ there is a dependence of $\Delta\Phi_0$ on the fill factor f and therefore also on the pitch. For increasing pitch at fixed CD, f approaches zero and so does $\Delta\Phi_0$. Interestingly, even for large pitches, the difference between $\Delta\Phi_0$ and $\Delta\Phi_1$ never approaches zero. Instead, it converges towards a finite value, which can be found by letting $\sigma \rightarrow 0$ in Equation (34) yielding

$$\Delta\Phi_1 - \Delta\Phi_0 = \lim_{\sigma \rightarrow 0} \Delta\Phi = \frac{\tilde{A}_{\text{eff}}}{\text{CD}} , \quad (36)$$

since $\lim_{x \rightarrow 0} x \cot(x) = 1$. This means that even for large pitches there is always a difference of $\frac{\tilde{A}_{\text{eff}}}{\text{CD}}$ between the phase differences of the zeroth and first diffraction order.

In Figure 8, we compare the phase difference of our approximate model according to Equation (34) with the results from rigorous calculations for a 300nm and a 500nm line. The agreement is remarkable, although the deviations from the rigorous results are somewhat larger for the 300nm line. We should stress again that both curves have been obtained with the same parameter \tilde{A}_{eff} , since the CD-dependence is given by $1/\text{CD}$.

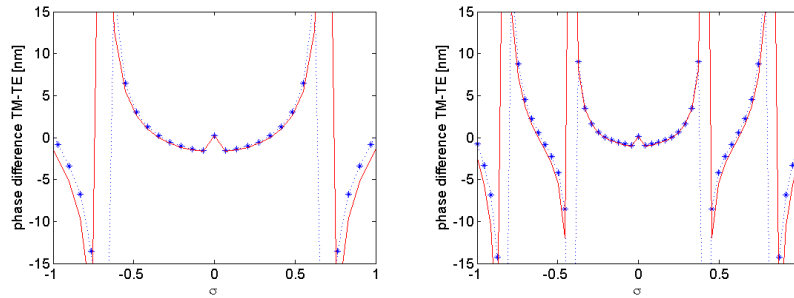


Figure 8. Comparison of the rigorous (blue dashed with asterisks) and approximate (red solid) results for a 300nm line (left) and a 500nm line (right).

6. EXPERIMENTAL RESULTS

Experiments to verify the polarization induced astigmatism effects of the mask have been performed on three different projection lens systems: The ASML TWINSSCAN™ XT:1400 (NA = 0.93), XT:1700i (NA = 1.2) and XT:1900i (NA = 1.35).

Figure 9a shows the experimental results on a ASML TWINSSCAN™ XT:1400. The structures under investigation were isolated 180nm Chrome H and V lines, illuminated by a y-polarized low sigma setting with $\sigma_{\text{outer}} = 0.22$ and reduced NA of 0.85. With a dose of about 30 mJ/cm², where the line prints to size, the focus shift is about 30nm. As energy increases the BF difference grows. At a dose of 45mJ/cm², one can find BF differences up to 300nm. Aerial image simulations in Figures 9b and 9c qualitatively confirm the experimental

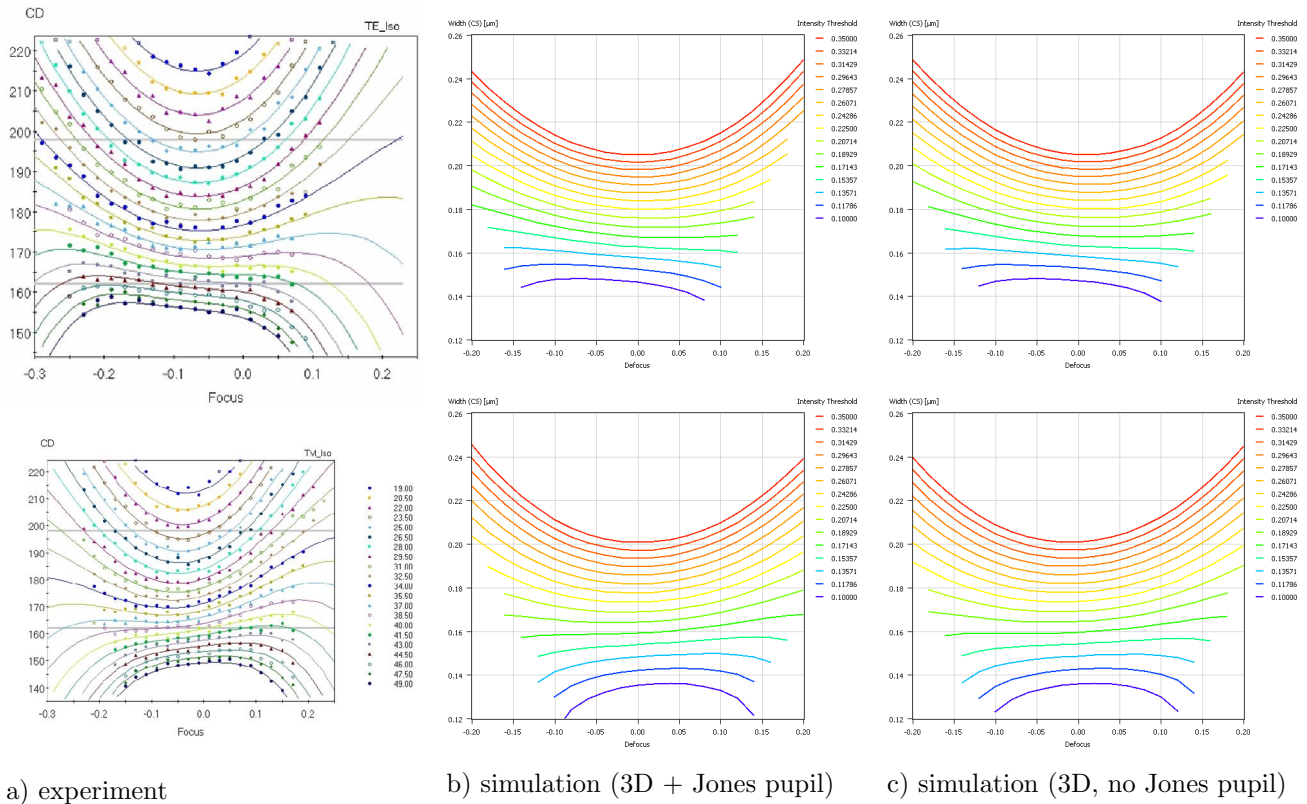


Figure 9. Experimental and simulated Bossungs for 180nm isolated Chrome lines on MoSi. Exposed with a XT:1400 at low sigma and linear y polarization. Upper row: V-line (TE polarization), Lower row: H-line (TM polarization).

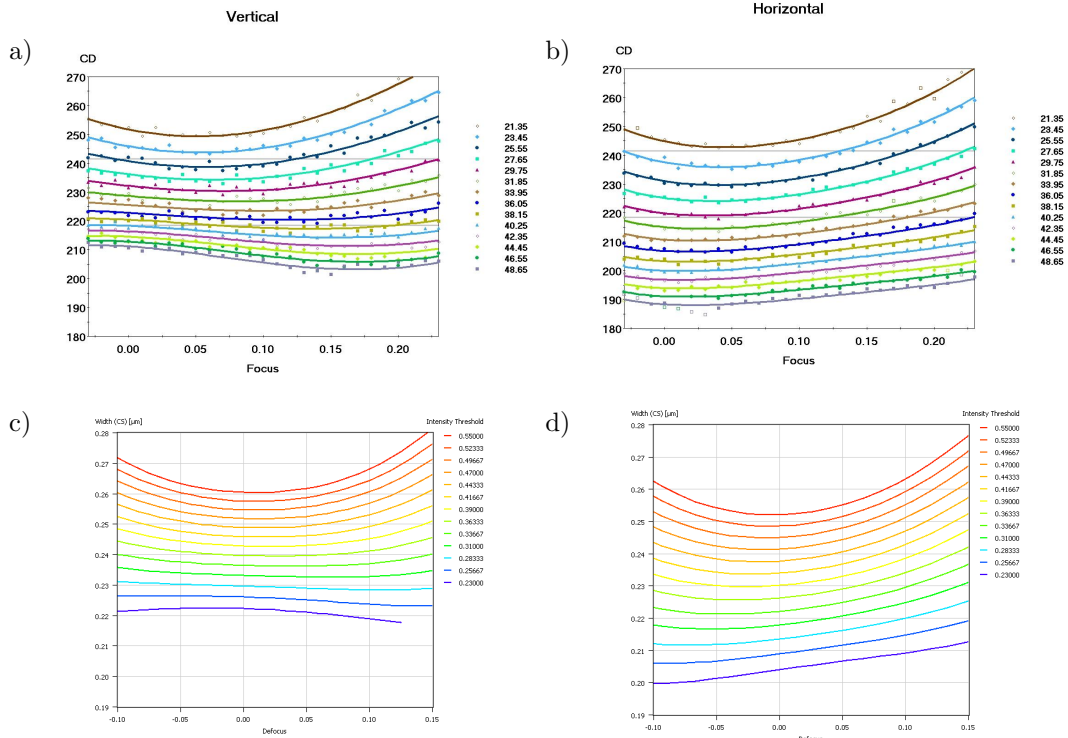


Figure 10. Bossung curves for 200nm vertical & horizontal isolated 6% MoSi lines on the XT:1700i exposed with low sigma and y polarization. a) and b) experimental data, c) and d) resist image simulations.

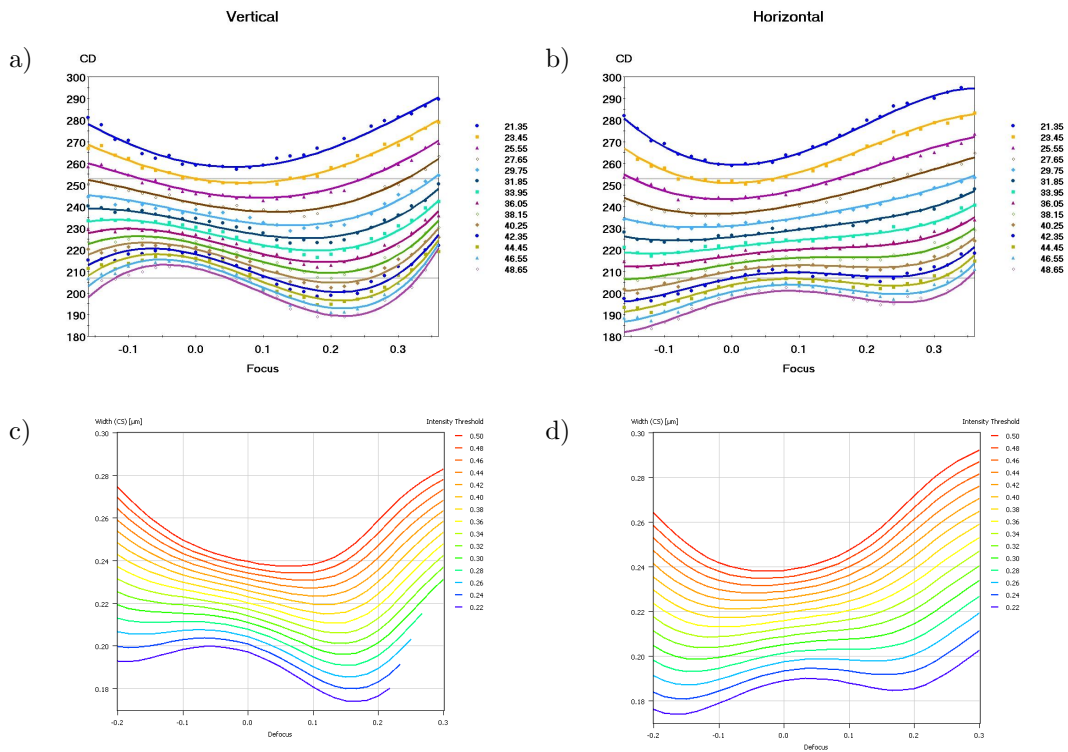


Figure 11. Bossung curves for 200nm vertical & horizontal isolated Cr lines on the XT:1700i exposed with low sigma and y-polarization a) and b) experimental data, c) and d) resist image simulations.

results. In Figure 9b the simulations were performed with a 3D mask and the lens Jones pupil, in Figure 9c the simulations were reran without the Jones pupil. Although the 3D mask simulations without the Jones pupil yield values which are similar to the experimental results, the simulations including the lens Jones pupil yield a better match.

The results obtained from the ASML TWINSCAN™ XT:1700i are presented for 200nm isolated lines in Figure 10, for a 6% MoSi AttPSM reticle, and in Figure 11 for a Chrome on Quartz reticle. Both reticles were imaged with a conventional source set to 0.17σ outer and linear y-polarization. In Figure 10, BF roughly shifts 100nm for vertical lines with an energy delta of $20\text{mJ}/\text{cm}^2$. For Figure 11, BF roughly shifts 200nm for vertical lines with an energy delta of $20\text{mJ}/\text{cm}^2$. The documented effect is twice as large for chrome on quartz as it is for 6% MoSi AttPSM. For the chrome on quartz reticle, a strong deformation of the Bossung curves can be observed. For higher values of dose, the Bossungs start to develop two extremes within the considered focus range, which makes the definition of a best focus ambiguous. Also notice the strong tilt of the Bossung curves around zero defocus. For both Figure 10 and Figure 11 subset c) and d) we plot matching aerial image simulations in resist using only the 3D mask effects. The agreement is remarkable.

In Figures 12 and 13 we show results obtained on the ASML TWINSCAN™ XT:1900i for both an isolated 200nm 6% MoSi feature and a chrome on MoSi feature, with the latter having an additional layer of 60nm Chrome on a 70nm MoSi base. Since the reticle only had vertical structures, the experiments were performed for x-polarized and y-polarized light. In addition unpolarized exposures were performed. The results for the 6% MoSi mask are shown in Figure 12. For the unpolarized case the Bossungs exhibit a symmetry about the point of best focus, with the focus being almost independent of dose. The polarized cases show a clear Bossung tilt in opposing directions which leads to a dose dependent BF delta. For Figure 13, the polarization effect on BF is much more pronounced for the 200nm chrome on MoSi. For the unpolarized case, some SEM data is missing. This is due to a non exposure related issue during data collection.

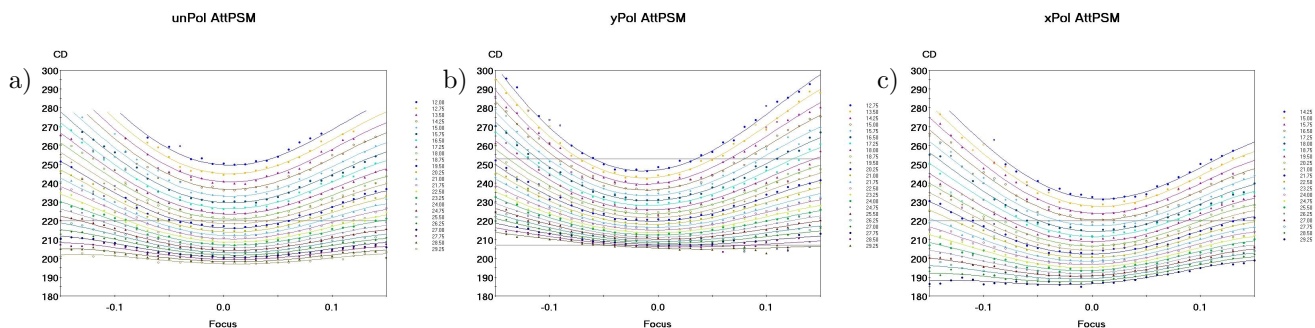


Figure 12. Experimental data obtained for 200nm vertical isolated 6% MoSi lines with the XT:1900i. a) unpolarized, b)y-polarized, c) x-polarized illumination.

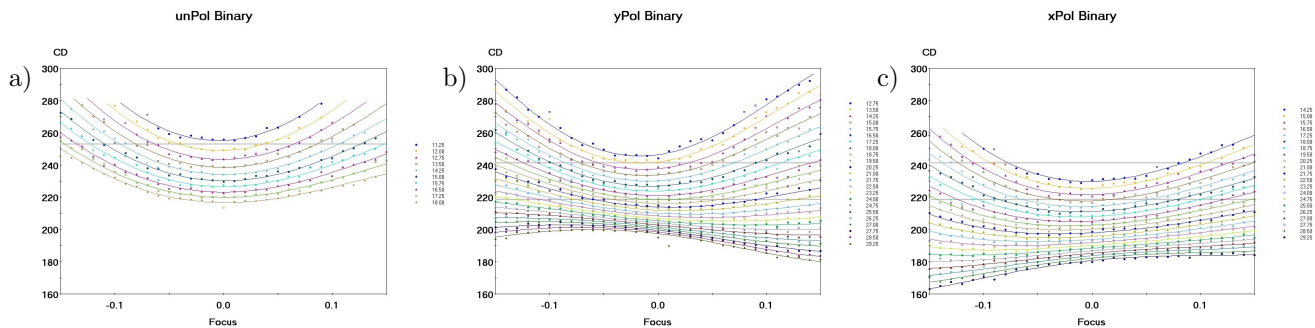


Figure 13. Experimental data obtained for 200nm vertical isolated chrome on MoSi lines with the XT:1900i. a) unpolarized, b)y-polarized, c) x-polarized illumination.

7. CONCLUSIONS

We have shown that for relatively large structures, topographic mask effects can have a nonnegligible impact on the lithographic performance, when used with polarized light. The finite thickness of the lines can influence the phases of the diffraction orders in such a way that it leads to a polarization dependent focus shifts. This polarization dependence translates into a best focus difference between horizontal and vertical lines, when printed at the same time using linear polarization in the illumination. As for unpolarized light, there is no focus difference, hence we can speak of polarization induced astigmatism due to 3D mask effects. We showed that these effects can be traced back to phase differences in the diffraction orders between TE and TM polarization. These differences are mainly caused by the vertical walls, where the boundary conditions for the electromagnetic field differ for TE and TM.

We introduced a simple extension of the Kirchhoff approach to account for these phase effects by adding two delta functions with a certain amplitude and phase at the step locations into the mask transmission function. For small amplitudes it turned out that the phase differences can be described by a single effective parameter, which depends only on the absorber material. This parameter has to be found through comparison with rigorous simulations, but once fixed for a given material, the phase effects can be computed with a remarkably high accuracy.

From the experiments and simulations, it became obvious that these phase effects can lead to strong polarization dependent distortions of the Bossung curves, causing large focus differences between horizontal and vertical lines. These focus shifts are combinations of a real defocus and focus shifts introduced by the tilting of the Bossung curves. As the position of best focus becomes particularly sensitive to the tilt in the isofocal region, seemingly large focus differences of several hundred nanometers can be obtained. It may even happen that the definition of BF becomes ambiguous, since the Bossung curves may have two local extrema. However, in this region, the Bossung curves are usually very flat, so that CD deviations with defocus stay rather small. Therefore, one must be cautious to use single Bossung curves to define BF, it is in this case rather more appropriate to use the center of the process window.

Nevertheless, it became obvious that even for large structures, is it not enough to include polarization effects from the lens or the illuminator and consider a Kirchhoff mask, since the mask effects may be of the same order or even stronger than the other polarization effects. As focus and CD budgets become ever tighter it therefore might become inevitable to also include 3D effects for the large and seemingly uncritical structures from the very beginning. As the computation time to solve Maxwell's equations strongly increases with the size of the considered structures, our approach to describe the phase (and amplitude) effects through simple analytic formulae may serve as a guideline to set up a modified Kirchhoff approach, which takes care of these polarization effects. Of course, the unknown parameters A and ϕ would have first to be found through comparison with rigorously computed diffraction coefficients, but as they only depend on the thickness and refractive indices of the lines, one would need only a few values, corresponding to a 6% MoSi or a Cr mask of a particular thickness.

In this study, we have not addressed possibilities of mitigating these phase effects. As the phase effects are strongly material dependent, it is conceivable that by choosing alternative mask materials the phase effects could be further reduced. Another possibility could be the coating of the side walls by some appropriate material or some combination thereof, which might have an inverse phase effect that could, at least to some extent, neutralize the polarization dependence. A third remedy could be to completely fill the spaces between the lines with either the blank material or some other appropriate transparent material. However, this remains to be studied in more detail.

ACKNOWLEDGMENTS

The authors would like to thank ASM Lithography, Robert Routh, Kevin Cummings and the College of Nanoscale Science & Engineering for supporting this research. Special thanks to the '1900 apps team' for performing the exposures on the XT:1900i, and Mariette Berende-Hoogendijk for the SEM measurements. We also thank Aksel Göhnermeier and Paul Gräupner for valuable input and discussions.

REFERENCES

1. A. Erdmann, "Topography effects and wave aberrations in advanced PSM technology," *Proc. SPIE* **4346**, p. 345, 2001.
2. A. Erdmann, "Mask Modeling in the Low k_1 and Ultrahigh NA Regime: Phase and Polarization Effects," *Proc. SPIE* **5835**, p. 69, 2005.
3. W. de Boeij, "Enabling the 45nm node by hyper-NA polarized lithography," *Proc. SPIE* **6154**, p. 61540B, 2006.
4. M. Totzeck, "How to describe polarization influence on imaging," *Proc. SPIE* **5754**, p. 23, 2004.

Practical use of hard mask process to fabricate fine photomasks for 45nm node and beyond

Yasuyuki Kushida^{*a}, Hitoshi Handa^{*a}, and Hiroshi Maruyama^{*a}
Yuuki Abe^{*b}, Yukihiro Fujimura^{*b}, and Toshifumi Yokoyama^{*b}
^aFujitsu Ltd.,
^bDai Nippon Printing Co., Ltd.,
2-2-1 Fukuoka, Fujimino, Saitama, Japan 356-8507

ABSTRACT

New process with hard-mask (HM) blanks was evaluated as one of candidates for photomasks beyond 45nm-node. Through the fabrication of gate-layer photomasks, aptitude of the HM process for practical use was confirmed from the view of controllability on CDs and defects. Although conventional process for attenuated PSM was shown to have critical CD error which belongs to the “patterns” in bright-field masks, experimental data proved effectiveness of the HM process to control CDs after process optimization. With the HM blanks, remarkable reduction of CD error more than 80% of conventional process was confirmed. In this report, peculiar opaque defects are also shown to be a critical issue on the HM process. From results of design of experiment (DOE), combining the proper means to prepare the HM blanks with the optimized HM etching condition, these defects were proved to be controlled within the tolerance for production. Through the investigations, validity of the HM process on practical use for mask fabrication of 45nm-node and beyond is considered as conclusions.

Keywords: 45nm-node, hard-mask (HM) blanks, bright-field masks, gate-layer, CD, defect

1. INTRODUCTION

As well known, advanced photomasks beyond 45nm-node require quite strict CD control. Especially, poor CD controllability of bright-field masks for gate-layer is recognized as one of the most critical issues to be overcome for their production.

Major part of CD errors in the bright-field masks has been made during Cr dry-etching process. In general, CD shift by dry-etching depends on Cr load, what is called “loading effect”. Lower etching selectivity in bright-field masks makes the etching bias larger and the situation much worse. Fig.1 is a typical example of Cr etching bias in bright field mask that shows the strong dependency on pattern pitch caused by “micro-loading effect” of Cr etching.

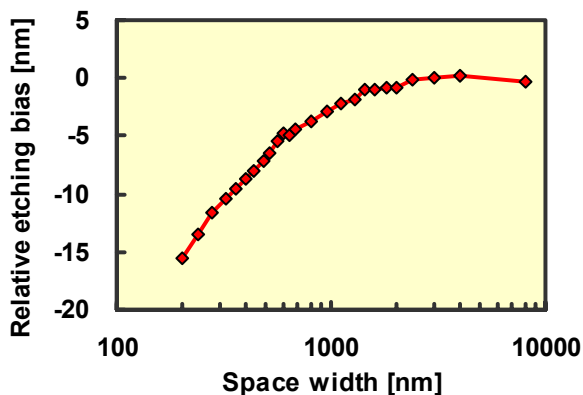


Fig.1 Dependency of Cr etching bias on pattern pitch (through-pitch)

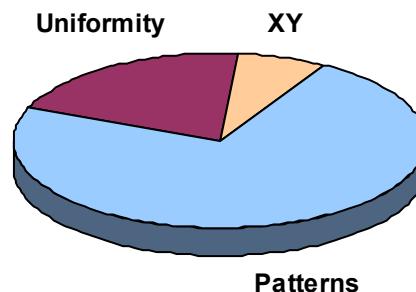


Fig.2 Analytical result of CD error components in gate-layer photomasks for 45nm-node

Fig.2 shows an analytical result of CD error components in the gate-layer photomasks fabricated in our production line. In this figure, CD error is classified into three categories, “Patterns”, “XY”, and “Uniformity”. It is clear that error on “Patterns”, CD difference among each pattern category (isolated-line, dense-line, SRAF, and so on), is the major part of the total error. As mentioned above, this error results from the property of Cr dry-etching which shows dependency on the pattern pitch. It is clear that error on “Patterns” should be much reduced to realize high CD controllability in bright-field masks. This is equivalent to eliminate the error on Cr etching due to “loading effect”.

Our goal in this study is to give a solution to the above “Patterns” issue for fabrication of fine photomasks beyond 45nm-node. In this report, new process using mask blanks with hard-mask (HM) layer was evaluated as one of promising techniques for this purpose.

There are several kinds of HM blanks proposed as materials for advanced photomasks. In this report, HM blanks based on MoSi attenuated PSM (attPSM) with TF-11 from HOYA were used. Investigations on their suitability for practical fabrication of gate-layer masks were performed from the view of controllability both on CDs and defects. Through the fabrication results, potential abilities of the new process were examined.

2. OUTLINE OF HM PROCESS

Structure of the HM blank used in this report is illustrated in Fig.3. Characteristic of the blank is its simple structure that inorganic HM layer is deposited on conventional Cr film, TF-11 (HOYA). In this report, MoSi based attPSM blanks were used for evaluation of CDs and defects because of their many actual results as a mask blank for ArF lithography.

Advantages of the HM blanks in mask fabrication are summarized as below,

- High etching durability of the HM layer against Cl_2/O_2 plasma enables to etch Cr film with high anisotropic conditions. This property is expected to reduce Cr etching bias and improve CD controllability.
- Design flexibility of the HM layer in film thickness and etching rate enables to adopt thin resist film less than 200nm. This property is expected to improve pattern resolution.

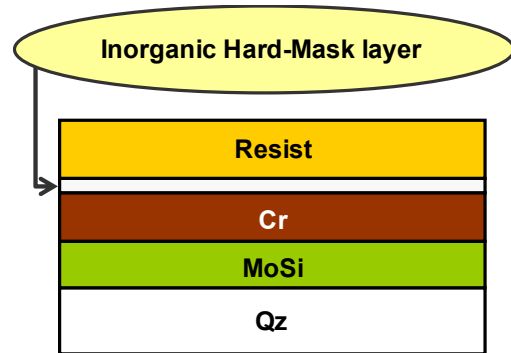


Fig.3 Structure of the HM blank

Process-flow of mask fabrication using HM blank is illustrated in Fig.4. HM blank is coated with thin resist film. Resist patterns are developed after conventional EB writing and PEB process. Any special treatments are not required in the resist process. After development, HM layer is etched by fluorine plasma using the resist-mask. At this step, Cr film under the HM layer is hardly etched because of its high etching durability against fluorine plasma. Cr dry-etching follows resist strip. At this step, Cr film is etched through the HM patterns using Cl_2/O_2 plasma. In this case, HM patterns act as perfect masks for Cr etching by their etching durability. HM layer is removed in following MoSi etching step using fluorine plasma at the same time. At this step, etching of the HM layer affects neither MoSi CD nor phase shift, because the HM layer is designed to be etched quite faster than MoSi. Unnecessary Cr film on MoSi is removed in final step.

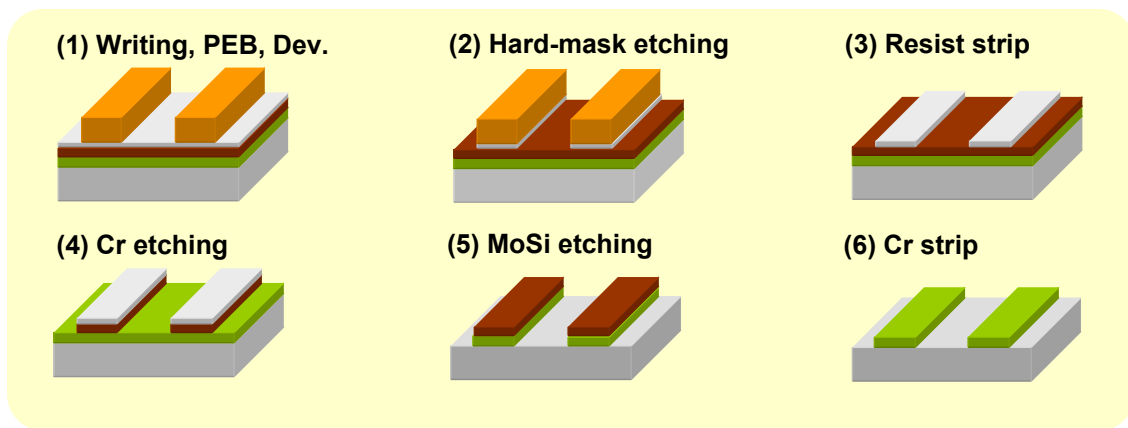


Fig.4 Process flow of mask fabrication using the HM blanks

3. EXPERIMENTAL CONDITIONS

To evaluate performance of HM process on CDs and defects, several test plates were fabricated with the assumption of practical mask production. Two kinds of MoSi attPSM blanks of HOYA (A61A-TF11), both with and without HM layer, were prepared. Thin Nega-CAR (NCAR) film was coated on the HM blank for fine pattern resolution. Thin resist film coating on the conventional blank is hard to be adopted, because of much resist erosion during Cr etching. Fig.4 illustrates the process flow of mask fabrication in this study.

Pattern inspections on CDs and defects were executed to verify whether the HM process had an aptitude for practical use or not. CD performance was checked with CD-SEM, LWM9000 (Vistec). Defect inspections were performed using LM7000B (NEC).

4. RESULTS AND DISCUSSIONS

4.1 CD PERFORMANCE

As a first step, dry-etching condition was optimized for bright-field masks, using the HM blanks coated with thin NCAR. Following in this section shows CD performance of the bright-field masks fabricated by the HM process. Reference data (Ref.) in this section means the results of conventional process using MoSi based attPSM blanks without HM layer.

4.1.1 DRY ETCHING PROPERTIES

Fig.5 shows the comparison of total etching bias between the two plates fabricated with the HM and the conventional (Ref.) process. In this figure, etching bias of each line pattern is normalized by result on the Ref. plate. In case of the HM process, remarkable reduction of etching bias as much as 80% of the Ref. plate is clearly seen. Moreover, dramatic decrease of iso/dense bias is also confirmed. This property is expected to improve CD results on through-pitch.

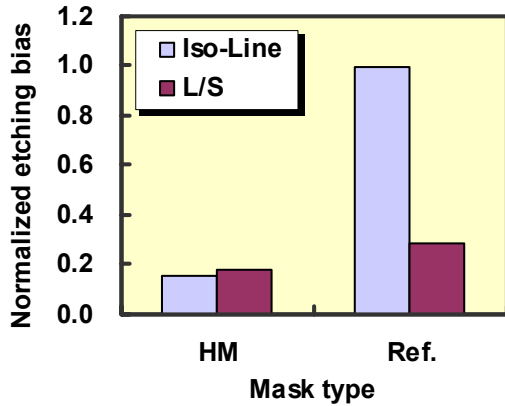


Fig.5 Comparison of total etching bias

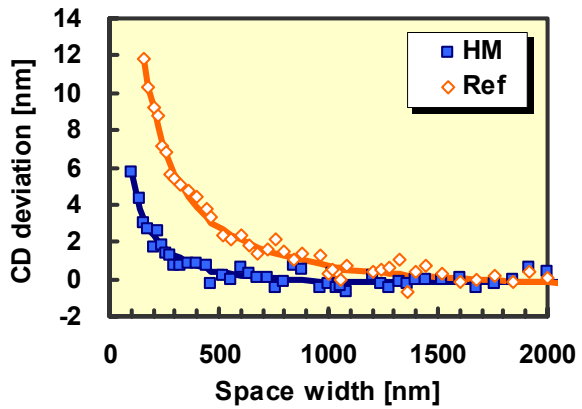


Fig.6 Comparison of MoSi CD through-pitch

MoSi CD property on through-pitch is shown in Fig.6. Through-pitch was measured on the 260nm lines for the pattern-pitch more than 360nm. Vertical axis in this figure means deviation of measured CD from target value (260nm). As clearly seen in this figure, the Ref. plate shows much steeper increase of CD value in the region of narrow pattern-pitch. CD range of the Ref. plate was 9.9nm for the space width from 2000 to 200nm. On the other hand, much reduction of CD range was confirmed in the HM plate. With the HM process, CD through-pitch was reduced to 3.2nm in this case.

Fine pattern resolution of dense-line for the each plate was observed with CD-SEM. This result is summarized in Fig.7. As seen in this figure, using the HM plate can improve pattern resolution down to 60nm. Combination of reduced etching bias with thin NCAR in this process gave this result.

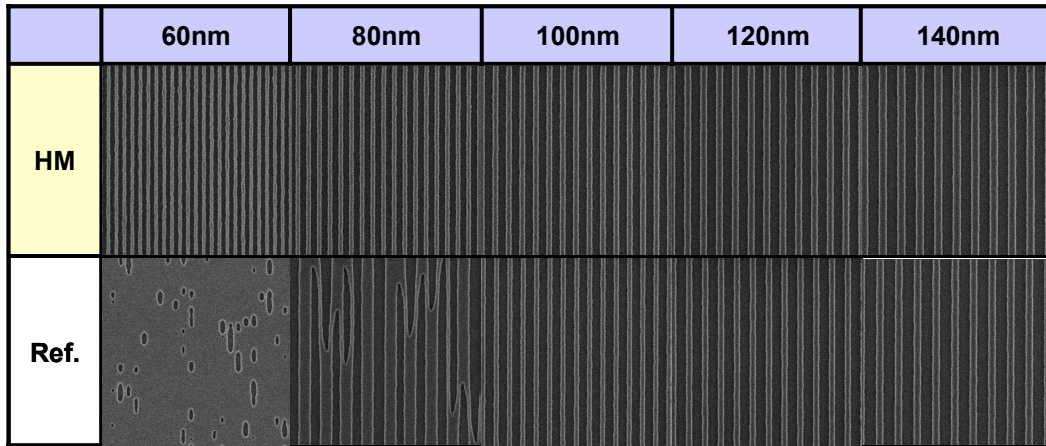


Fig.7 Comparison of SEM images of the dense lines of MoSi between the HM and Ref. plate

4.1.2 CD RESULT OF 45NM-NODE GATE LAYER

As described above, dry-etching properties on bright-field masks can be improved dramatically with the HM process. For the next step, trial fabrications of the photomasks for 45nm-node gate-layer were accomplished to investigate the above effects on CDs, such as through-pitch and CD difference among each pattern category.

Fig.8 shows the through-pitch results in the gate-layer mask. CDs were measured for the lines with SRAF whose target sizes were from 280nm to 400nm. Minimum pattern-pitch was 520nm in this case. Values on the vertical axis mean CD

deviation as Fig.6. From this figure, CD range in the Ref. plate is evaluated as 7.0nm. This result was caused by the CD deviation between isolated-line and the dense-line of medium pattern-pitch. In the HM plate, this CD deviation was almost removed. This result is understood from the CD data in Fig.6.

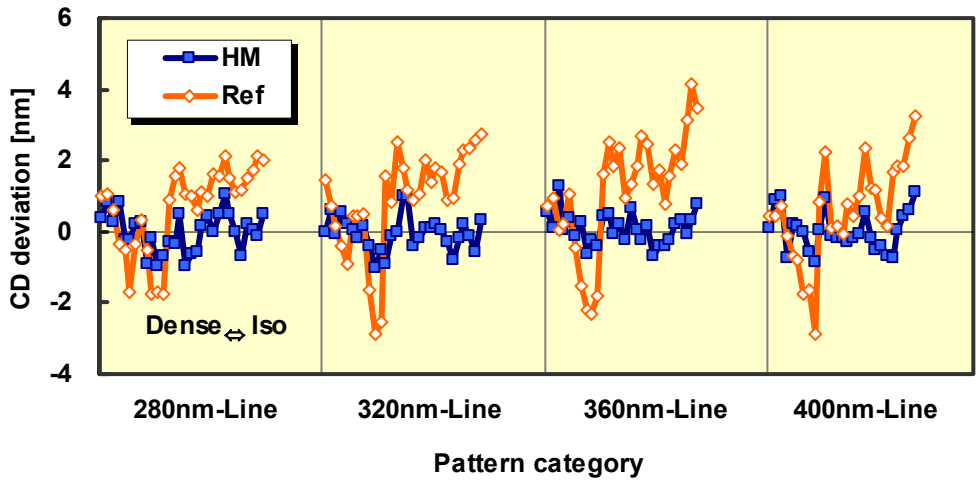


Fig.8 Comparison of MoSi CD through-pitch between the HM and Ref. plate

CD deviations among different pattern categories were also investigated. CD of ten kinds of pattern categories, such as Iso/Dense-Line, SRAF, and line-tip and so on, were measured with CD-SEM. CD of each category was evaluated using the average of five points' data within the plate. Evaluated pattern categories are illustrated in Fig.9.

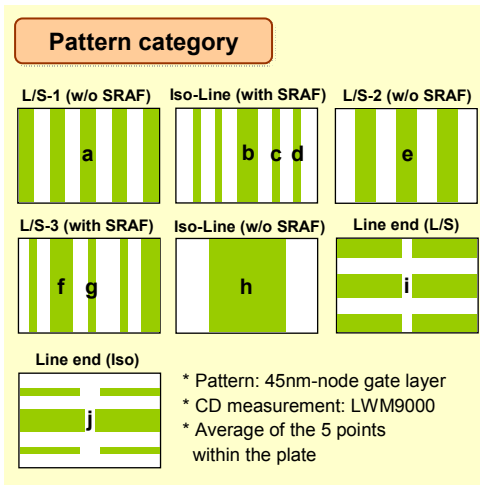


Fig.9 Pattern categories for CD evaluation

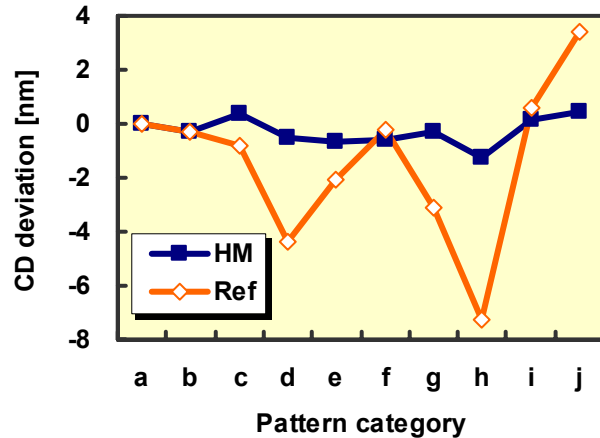


Fig.10 Comparison of CD deviations between each category

Fig.10 shows CD variation depending on the pattern categories. In the Ref. plate, peculiar deviations at pattern-d, -h, and -j, were observed. They correspond to the outer SRAF, isolated-line without SRAF, and neighbored line-end, respectively. On the other hand, no peculiar deviation was observed for the HM plate. CD range among all pattern categories was 10.6nm for the Ref. plate and 1.7nm for the HM plate, respectively. This result implies that CD errors depending on the device patterns in bright-field masks are almost vanished through the HM process.

4.1.3 DISCUSSION ON CD PERFORMANCE

As shown in above sections, CD performance of bright field mask could be much improved with HM process.

High etching durability of HM layer helped to control Cr etching bias without shrinking of the mask patterns for etching. Moreover, quite thin HM layer less than 10% of conventional resist film was also effective to prevent CD deviation due to “micro-loading effect”, because of lower aspect ratio in the line patterns with narrow pitch.

HM blanks enabled to adopt the Cr etching condition of high anisotropy which had been hardly permitted to the conventional NCAR blanks. Adoption of this condition was also effective to reduce etching bias and repress the loading effect.

In conventional process, pattern resolution had been limited due to collapse of resist patterns during the development. Use of the HM blanks realized the etching process with thin resist film which was also effective to prevent the collapse due to high aspect ratio and improve pattern resolution.

As explained, issue on the CD controllability can be solved with the HM process. CD error caused by “Patterns” was reduced so much that capability of the process was proved to be high enough to fabricate gate-layer photomasks for 45nm-node.

4.2 DEFECT DENSITY

As well-known, fabrication of advanced photomasks is required high controllability of defects as well as CDs. In following sections, results on defect inspection of the HM plate and process trial to control the defects are described.

4.2.1 ISSUE FOR BEYOND 45NM-NODE

After defect inspection on the HM plate, defects of peculiar mode had been often detected. Fig. 11 shows the SEM image of one of the defects. They were extended opaque defects smaller than 100nm and had never been seen in the conventional process for attPSM with same resist. Considering the difference between the two processes, it was probable that combining of the NCAR with the HM blanks caused the defects.

Our investigations indicated that “scum” and “line edge roughness” of the NCAR had close relationship to the defects. In this case, scum of the resist acts as mask for the HM etching the same as the resist itself. It causes the above extension defects, when erosion of the scum during the process is insufficient. NCAR process, which leaves the scum easily on the HM layer, is probable to be an origin of the defects. It is no doubt that these defects are killer ones for the advanced masks beyond 45nm-node, and have to be removed perfectly.

To prevent the generation of defects, some means how to prepare the HM blanks had been examined. Three parameters, strength of adhesion between the NCAR and HM layer (Resist Adhesion Force), bake temperature after resist coating (Pre-Bake Temp.), and bake temperature after EB writing (PEB Temp.), were focused. Best combination of these parameters was examined to eliminate the above peculiar defects from HM plates.

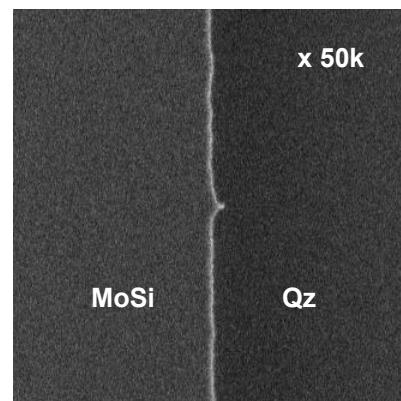


Fig.11 Peculiar defects of the HM process

4.2.2 PROCESS OPTIMIZATION FOR DEFECT REDUCTION

Design of experiment (DOE) was planned to investigate the best condition of blank preparation. Table.1 shows the DOE table using three parameters with two levels in this experiment. As seen in this table, four test plates were prepared to check the effects of each combination on line edge roughness and count of the peculiar opaque defects. Layout of the test plate is illustrated in Fig.12. Die-to-die defect inspections were performed on the five areas composed of 200nm dense lines. Each area was written with the different levels of EB dosage. This idea is useful to compare the effects of each parameter among the areas of same CD, considering variation of the resist sensitivity to bake temperature. In this experiment, line edge roughness was evaluated as 3 sigma of line width roughness (LWR) measured by CD-SEM.

Table.1 Combination of process conditions in DOE

Plate	Resist Adhesion force	Pre-Bake Temp.	PEB Temp.
A	Low	High	High
B	Low	Low	Low
C	High	Low	High
D	High	High	Low

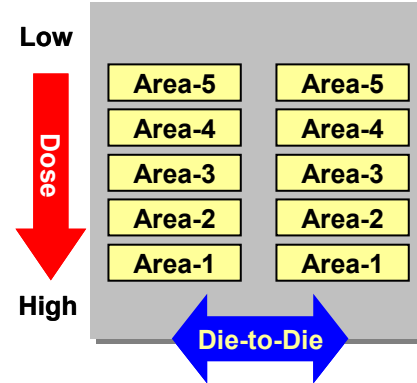


Fig.12 Layout of the test plates

Effect of each parameter is summarized in Fig.13. Variation of the defect count and LWR are converted into S/N ratio defined as below,

$$S/N \text{ Ratio} = -10 \times \log \frac{a_1^2 + a_2^2 + \dots + a_N^2}{N} \text{ [db]} \quad (1)$$

In this equation, N is the number of measurement data, and a_1, a_2, \dots, a_N correspond to the each data, respectively. From the definition of S/N ratio, it takes larger value when the defect count or LWR is reduced and the average of squared data becomes smaller. Larger S/N ratio means preferable effect in short.

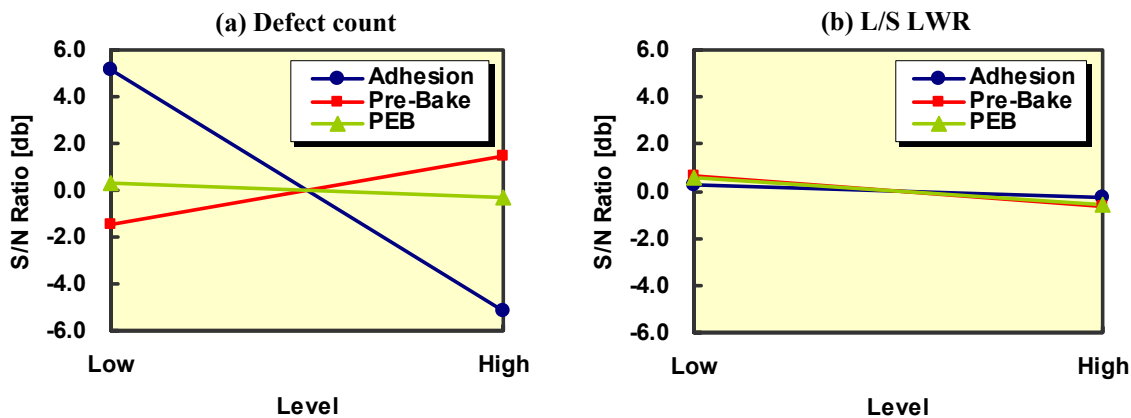


Fig.13 Effect of each process factor on (a) Defect count, (b) L/S LWR

From the Fig.13 (a), both resist adhesion force and pre-bake temperature are shown to be effective parameters to control the defects. Combination of lower adhesion force with higher pre-bake temperature is expected to reduce defect count so much. On the other hand, PEB temperature shows negligible effect on defect count.

Fig.13 (b) shows the effect of the three parameters on control of LWR. As clearly seen, LWR is not almost affected by the parameters. This result implies that control of LWR by the three parameters is hardly expected its effect and other means should be done for this purpose.

From the minute consideration of the above results, one simple relationship among defect count and the process parameters was derived. This is expressed as below,

$$[Defect\ count] = a \times [Adhesion] + b \times [Pre-Bake] + c \times [L/S\ LWR] + d \quad - (2)$$

In this equation, coefficient *a*, *b*, *c*, and *d* are constants decided from experimental results. In this case, both *a* and *b* showed minus sign, while *c* showed plus.

One noticeable relationship that defect count depends on the LWR is clearly seen in equation - (2). This relationship is summarized in Fig.14 (a) and (b). From comparison of the R^2 value between Fig.14 (a) and (b), adding the effect of L/S LWR into the equation is proved to explain the results of defect count better. This result implies the importance of LWR control to reduce the defect count, as well as optimization of resist adhesion force and pre-bake temperature. Improvement of L/S LWR is a critical factor to reduce the defects, in other word.

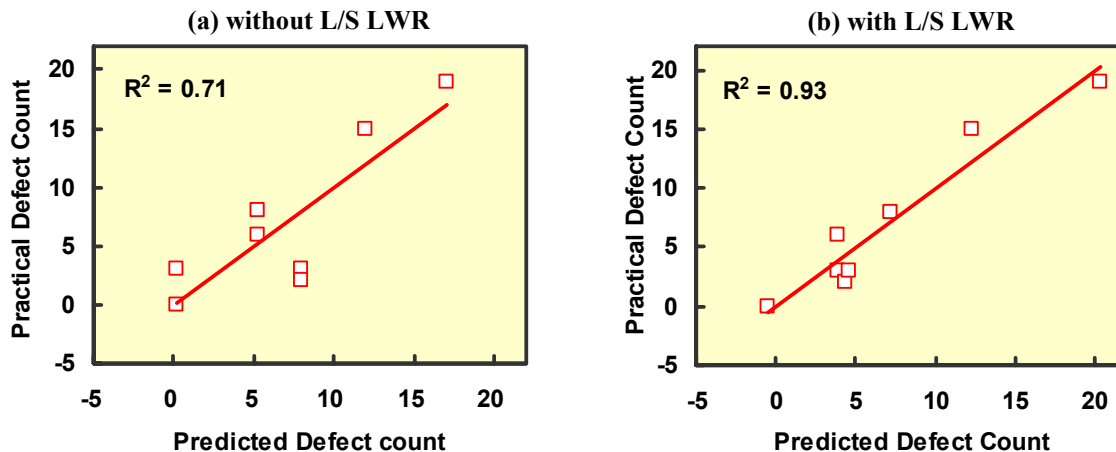


Fig.14 Relationship between practical defect count and its prediction, (a) without L/S LWR, (b) with L/S LWR

Based on the DOE results, both surface treatment of the blanks and pre-bake temperature were optimized to eliminate the scum of NCAR. L/S LWR was reduced through the re-examination of etching condition of HM layer. Fig.15 shows the defect inspection results on the bright-field masks after process optimization. Vertical axis of the right side means normalized LWR value. As expected, defect count decreased along with reduction of LWR. After optimization of the HM etching, sample#5, only one defect was detected with the minimum LWR value. This result confirmed that our new process enabled to control defects on the HM plate within the tolerance for practical fabrication of bright-field masks.

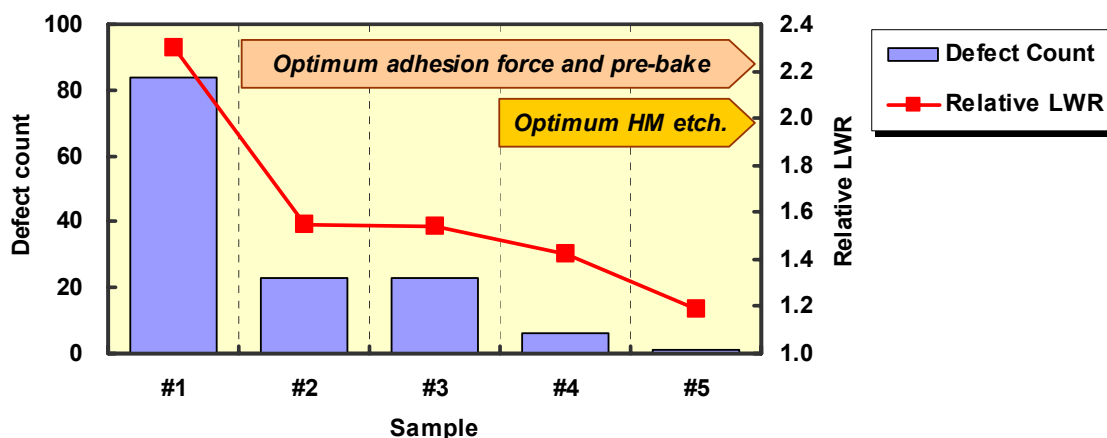


Fig.15 Transition of defect count and LWR along with the process optimization

4.2.3 DISCUSSION ON DEFECT DENSITY

In this study, process condition was optimized to reduce defect count of HM process to the level of tolerance for practical use. From the DOE results, combination of proper preparation of HM blanks with optimized HM etching was confirmed its effectiveness to control the defects.

As for the preparation of the HM blanks, surface treatment before resist coating was one of critical factors to control the adhesion force of NCAR on the HM layer. On the other hand, bake temperature after resist coating was assumed that it could control solubility of the NCAR to the developer. Best combination of these parameters was probably useful to suppress the generation of the scum without collapse of resist patterns.

L/S LWR, which did not depend on how to prepare the blanks, was experimentally proved to be another critical factor for defect reduction. Re-examination of the HM etching was effective to reduce LWR. Increase of resist erosion within the tolerance of CD variation was a key factor to improve the LWR and eliminate the peculiar defects in the HM plate. With the optimized etching condition, defect count could be reduced to the level of practical use for mask fabrication.

5. CONCLUSIONS

To establish the method to fabricate the bright-field photomasks beyond 45nm-node, aptitude of the new process using the HM blanks was evaluated from the two aspects, CDs and defects. It was confirmed that dry-etching properties, such as etching bias and through-pitch, were much improved by the HM process with combination of thin NCAR with anisotropic Cr etching. As a result, CD difference among each pattern category in the gate-layer photomask was reduced from 10.6nm to 1.7nm.

Investigations on how to control the peculiar opaque defects in HM process were carried out through the DOE. It was found that reduction of LWR was a critical factor to control the defects, in addition to blanks preparations in surface treatment of the HM and pre-bake temperature of the NCAR. With best combination of above conditions, detected defects were reduced to the level within the tolerance for practical fabrication.

Process with the HM blanks is a most powerful technique and ready for practical fabrication of gate-layer photomasks for 45nm-node, proving its ability to control CDs and defects. Process optimization on controllability of the extension defects will be a subject for the generation beyond 45nm-node. Another NCAR as substitution of the present one is expected to be a solution for this issue.

6. ACKNOWLEDGEMENTS

We would like to thank Mr. Y. Okubo and Mr. A. Kominato of HOYA Corporation for their technical support to this study. We would also like to thank Mr. Y. Miyahara and Mr. N. Ishiwata of Fujitsu Ltd., and Mr. T. Furukawa of Dai Nippon Printing Co., Ltd., for their meaningful advice to this study.

7. REFERENCES

1. Y. Abe., et al., "Multi-layer resist system for 45nm-node and beyond (III)," *Proc. of SPIE*, vol. 6349, 2006
2. Y. Fujimura., et al., "Multi-layer resist system for 45nm-node and beyond (II)," *Proc. of SPIE*, vol. 6349, 2006
3. M. Hashimoto., et al., "Multi-layer resist system for 45nm-node and beyond (I)," *Proc. of SPIE*, vol. 6349, 2006